A study of charm mixing





Kamil Fischer

St Anne's College

University of Oxford

Michaelmas Term, 2024

A thesis presented for the degree of
Masters by Research

Abstract

A feasibility study has been conducted to investigate the potential measurement of charm mixing parameters using a model independent approach known as the bin-flip method applied to the $D^0 \to K^0_S K^+ K^-$ decay mode for the first time at LHCb. This study utilises proton-proton collision data collected at a center-of-mass energy of $\sqrt{s} = 13$ TeV and corresponding integrated luminosity of 5.7 fb^{-1}.

Contents

1 Introduction **4**

2 Theoretical background **5**
2.1 The Standard Model . . . 5
2.2 Discrete symmetries . . . 6
2.3 CP-violation . . . 7
2.3.1 The GIM mechanism . . . 8
2.3.2 The CKM matrix . . . 9
2.4 Neutral meson mixing . . . 11
2.5 Classification of CP-violation . . . 14
2.5.1 CP-violation in the decay . . . 15
2.5.2 CP-violation in mixing . . . 15
2.5.3 CP-violation due to the interference between decay and mixing . . . 16
2.6 Self conjugate multi-body final states . . . 16
2.7 Measuring charm mixing parameters with the bin-flip method . . . 17
2.7.1 Formalism . . . 18
2.8 Quantum-correlated $D\bar{D}$ decays . . . 20

3 The Large Hadron Collider (LHC) and the LHCb experiment **21**
3.1 The Large Hadron Collider (LHC) . . . 21
3.2 The LHCb detector . . . 22
3.3 The LHCb trigger . . . 24

4 Data selection and reconstruction **26**
4.1 Production modes . . . 26
4.2 Selection criteria . . . 27
4.3 Prompt sample . . . 29
4.3.1 L0 requirements . . . 29
4.3.2 HLT1 requirements . . . 29
4.3.3 HLT2 and offline selection . . . 30
4.4 Semileptonic sample (SL) . . . 33
4.5 Determination of signal yields . . . 37
4.6 Comparison with $D^0 \to K^0_S\pi^+\pi^-$ decays . . . 40
4.7 Detector resolution . . . 41
4.8 Efficiency variation as a function of decay-time . . . 43
4.9 Efficiency variation across the Dalitz plot . . . 44
4.10 Correlations between decay-time and Dalitz plot efficiencies . . . 46

5 Fits to data **51**
5.1 Signal yield extraction . . . 51
5.2 Determination of $\langle t \rangle$ and $\langle t^2 \rangle$ . . . 51
5.3 Determination of mixing parameters . . . 51
5.4 Results . . . 54

6 Future work **55**
6.1 Systematic uncertainties 55
6.2 Future improvements 58

7 Conclusion **58**

1 Introduction

The Standard Model (SM) of particle physics describes fundamental particles and their interactions, with its predictions of the electron magnetic moment experimentally verified to $\mathcal{O}(10^{-12})$ [1]. The recent discoveries of the top quark [2, 3], the tau neutrino [4] and the Higgs boson [5, 6] further cement its validity. Despite the many triumphs, the SM is incomplete. The theory does not incorporate gravity nor does it provide any dark matter candidates necessary to account for cosmological observations [7]. Most strikingly, the observed universe is a matter dominated cosmos rather than a vast expanse of radiation, primarily photons produced by annihilation of primordial matter and anti-matter. In such a scenario electrons and quarks emerge through pair production, however are insufficiently long lived to form stable structures [8]. Investigating mechanisms responsible for differences between particles and anti-particles, such as charge-parity (CP) violation, provides a path towards a complete understanding of a matter dominated universe.

The field of flavour physics, particularly the study of neutral mesons, is an ideal laboratory for the discovery of phenomena beyond the SM that could explain the observed matter anti-matter asymmetry. Due to the noncoincidence of mass and flavour eigenstates, oscillations govern the time evolution of neutral mesons. In the SM, a flavour oscillation occurs either via weak interaction processes mediated by the exchange of virtual $W^{\pm}$ bosons and heavy quarks or through long distance scattering. In the charm sector, short range contributions are suppressed by the GIM mechanism, thus long distance scattering processes dominate [9, 10]. A virtual particle of an arbitrary mass, which participates in the exchange, will contribute to the decay amplitude and may potentially enhance the rate of oscillation or the difference between transition rates. As such, flavour oscillations are a sensitive probe of physics beyond the SM since CP violation is expected to be small $\mathcal{O}(10^{-3})$ but could be enhanced by new phenomena [11–15].

Although oscillations have long been established in other neutral meson systems $K^0 - \bar{K}^0$ [16], $B^0 - \bar{B}^0$ [17] and $B_s^0 - \bar{B}_s^0$ [18], the first observation of $D^0 - \bar{D}^0$ oscillations has only been performed in the last decade [19]. In recent years, the LHCb collaboration has observed direct CP violation in the charm sector by studying $D^0 \to h^+h^-$ decays ($h = K, \pi$) [20]. Such an effect has not been observed in mixing phenomena (indirect CP violation), further motivating studies in this area.

Measurements of the decay-rate of multibody self-conjugate decays such as $D^0 \to K_S^0\pi^+\pi^-$ and $D^0 \to K_S^0K^+K^-$ allow for a determination of mixing and CP-violating parameters. By simultaneously considering the decay-time and phase-space distributions, a component initially produced as D^0 or $\bar{D}^0$ can be identified and the evolution can be studied. Such an approach requires a good understanding of the variations of strong-phase differences across this phase-space. The strong phase information can be determined using an amplitude model. However, to avoid model dependence in the analysis, auxiliary measurements of strong phases performed by CLEO-c and BESIII at the charm threshold are utilised [21, 22]. Strong-phase information is equally important in measurements of the CKM angle γ using $B^{\pm} \to D^0K^{\pm}$,$D^0 \to K_S^0h^{\pm}h^{\mp}$ decays [23]. This thesis studies the feasibility of measuring charm mixing parameters using $D^0 \to K_S^0K^+K^-$ decays at LHCb for the first time.

2 Theoretical background

2.1 The Standard Model

In the SM, the strong, weak and electromagnetic interactions comprise the three forces that govern particle interactions. The SM does not incorporate gravitation which is the fourth fundamental force. The strong interaction confines quarks inside of hadrons as well as binds protons and neutrons to form atomic nuclei. The weak force provides the mechanism responsible for radioactive decays of atoms. In addition, the dynamics of electrically charged particles are governed by the electromagnetic interaction.

The building blocks of the SM are presented in Fig. 1. Elementary particles are categorised either as fermions, with half-integer spin, or as gauge bosons, particles with integer spin.

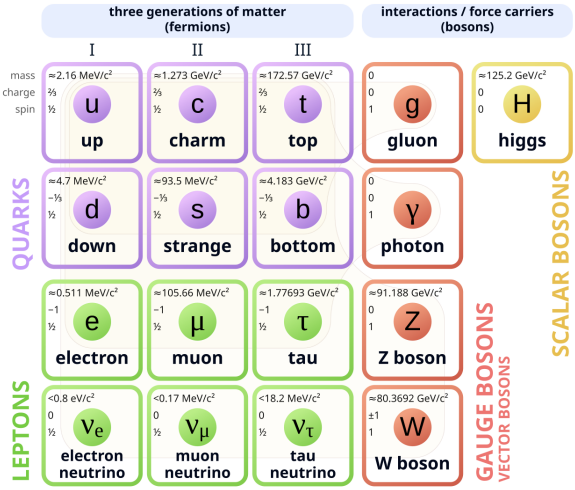


Figure 1: Schematic representation of elementary particles in the Standard Model [24].

In the SM there exist three generations of fermions separated into two classes: quarks and leptons. Each generation contains an up-type quark that has a charge of $\frac{+2}{3}e$ and a down-type quark with a charge given by $\frac{-1}{3}e$. The quarks are sensitive to all three of the fundamental forces. In addition, each generation contains a charged lepton, electron-like with a charge of $-1e$, and an associated neutral partner known as the neutrino. Charged leptons interact through both the electromagnetic and weak interactions whilst neutrinos are only sensitive to the weak interaction. For each there exists a corresponding anti-particle with an identical mass and opposite sign for quantum numbers such as charge. The second and third generations of leptons follow an identical structure with masses increasing across generations. Although in the SM neutrino masses are assumed to be zero, observed oscillations require at least two of the three generations of neutrinos to have a non-zero mass [25].

The gauge bosons are the force carriers exchanged during particle interactions. The strong force is mediated by eight massless gluons, each corresponding to a specific combination of color-anticolor charges. The $W^{\pm}$ and Z^0 bosons carry the weak force, mediating flavour changing processes and particle decays. These bosons gain their mass through a

coupling to the Higgs boson, an excitation of the Higgs field. Electromagnetic interactions occur through the exchange of a massless photons between charged particles.

In the SM hadrons are structures of more than one quark bound in a colour neutral state. Baryons comprise of at least three quarks (red-blue-green), whilst mesons consist of quark-antiquark pairs (colour-anticolour). The majority of the visible matter in the universe is baryonic, first generation quarks bound together tightly to form protons and neutrons. More complicated hadronic structures are possible as shown by the recent discoveries of pentaquarks at LHCb [26].

2.2 Discrete symmetries

Symmetries are critical to the structure of physical laws. According to Noether's theorem, each continuous symmetry of the action that remains invariant under a transformation corresponds to a conserved quantity associated with that transformation [27]. The invariance of the SM under spatial and temporal translations leads to conservation of momentum and energy, respectively. Whilst gauge invariance leads to conservation of current. As such, symmetries allow for an understanding of fundamental forces in a unified manner. Additionally, symmetry principles can assist in the search for physics beyond the SM.

A discrete transformation is a non-continuous change of a system. In the SM there exist three such symmetries:

- The charge conjugation transformation (C) flips the sign of all additive quantum numbers such as charge and lepton number, transforming a particle into the corresponding anti-particle. The reverse also holds.
- The parity transformation (P) acts by inverting all spatial coordinates of a particle such that $x \to -x$ and $\vec{p} \to -\vec{p}$.
- The time reversal transformation (T) inverts a particles temporal coordinates, $t \to -t$.

The individual symmetries posses an associated operator, which when acting upon a state produces even and odd eigenvalues given by ± 1. Additionally, any Lorentz-invariant quantum field theory is conserved under the combined CPT transformation. [28]. This implies that the mass and lifetime of a particle must be identical to that of the corresponding particle.

In the SM, the strong and electromagnetic interactions are found experimentally to be invariant under all combinations of the C,P and T transformations. In 1956 an experiment was proposed by C.N. Yang and T.D. Lee to test the P symmetry in weak interactions. At the time, the K_S^0 and K_L^0 particles were observed to exist with identical properties, however decayed weakly into final states of opposite parity [29]. This observation hinted at the non conservation of the P symmetry. The analysis of beta decays of Cobalt-60, conducted by C.S. Wu et al, observed that the production probability of a weak decay process differed from that of the mirror image. Thus confirming the violation of the P-symmetry [30]. In the SM, the weak charged currents, $W^{\pm}$, only couple

to left-handed fermions and right-handed anti-fermions. Therefore the individual C and P symmetries are maximally violated since it is the combined CP transformation that converts a left-handed fermion into a right-handed anti-fermion. In 1964 J.W. Cronin and V.L. Fitch studied decays involving neutral kaons. These experimental observations established the breaking of the CP sysmmetry [31], giving rise to the study of CP violation. Such a discovery implies the breaking of the individual T symmetry since the combination of CP and Tmust be conserved. The non-conservation of the T symmetry has been experimentally verified by the CPLEAR experiment [32].

The breaking of the CP symmetry is a potential solution to the observed baryonic matter asymmetry. In the early universe, baryogenesis preferentially produced matter. Though the asymmetry was small, $\mathcal{O}(10^{-9})$, the consequence is a universe filled with particles rather than anti-particles. CP-violation is one of the three Sakharov conditions necessary for baryogenesis [33]:

1. There must exist processes in the SM that violate baryon number conservation thus producing an excess of baryons.

2. Both the C and CP symmetries must be violated. This ensures that for every process that produces an excess of baryons there does not exist a corresponding process that produces an excess of anti-baryons.

3. There must exist a phase of rapid expansion in the universe such that interactions occur out of thermal equilibrium. If the rate of reactions responsible for generating the baryon asymmetry is slower than the rate of expansion of the universe, interactions involving baryon number violation and CP violation have insufficient time to reach thermal equilibrium. As a result, particles and antiparticles cannot annihilate in a way that would restore symmetry.

The SM incorporates both C and CP violation. However, the size of these CP-violating effects is by itself insufficient to explain the observed baryonic matter asymmetry. Therefore studying CP-violating mechanisms could reveal physics beyond the SM.

2.3 CP-violation

In the SM quarks can change flavour through the exchange of $W^{\pm}$ bosons, allowing for an up-type quark to change flavour into a down-type quark. In contrast, strong and electromagnetic processes couple exclusively to quarks and leptons within the same generation. In the Cabibbo hypothesis the weak eigenstates, d' and s', are related to the mass eigenstates by a unitary matrix,

$$\begin{bmatrix} d' \\ s' \end{bmatrix} = \begin{bmatrix} \cos\theta_c & \sin\theta_c \\ -\sin\theta_c & \cos\theta_c \end{bmatrix} \begin{bmatrix} d \\ s \end{bmatrix}, \tag{1}$$

where θ_c is the Cabibbo angle. The weak eigenstate, d', is a superposition of the down, d, and strange, s, quarks. Similarly for the s' [34]. The Cabibbo mechanism allows for flavour changing neutral currents (FCNC) to occur. Examples include $K_L^0 \to \mu^+\mu^-$ decays and $K^0 - \bar{K^0}$ mixing, which can proceed via the exchange of a virtual up quark. The corresponding Feynman diagrams are shown in Fig. 2.

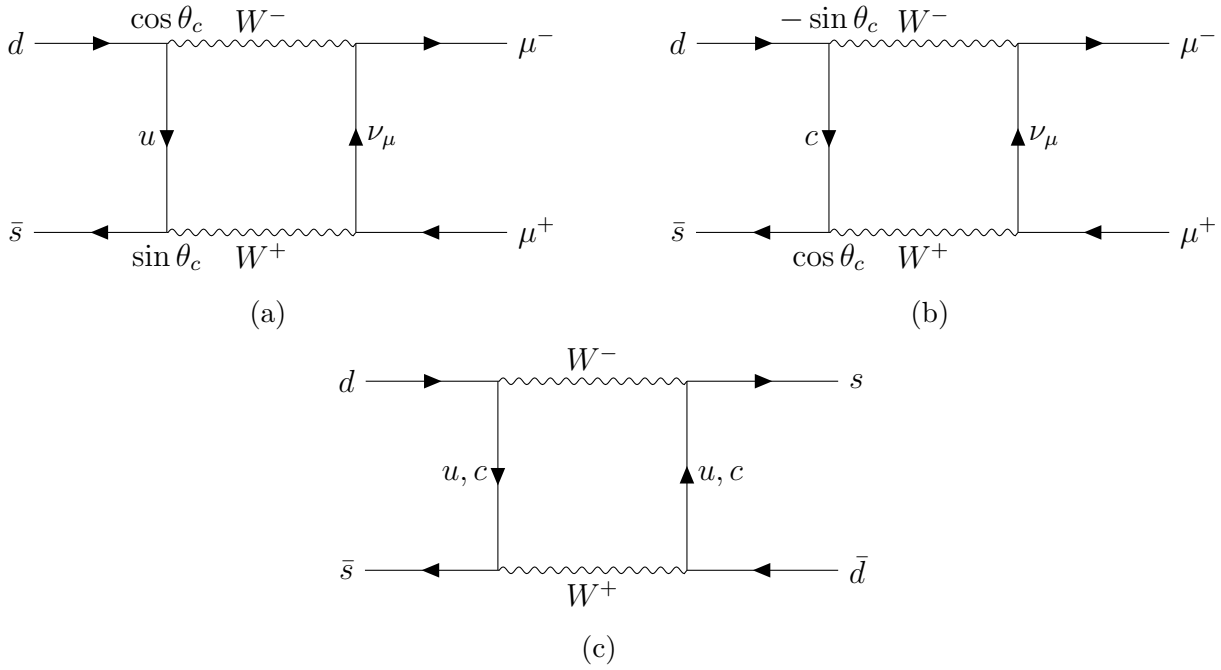


Figure 2: (a) $K_L^0 \to \mu^+\mu^-$ decays prior to the introduction of the charm quark. (b) Contribution of the charm quark to $K_L^0 \to \mu^+\mu^-$ decays. (c) Feynman diagram showing $K^0 - \bar{K^0}$ mixing.

2.3.1 The GIM mechanism

The GIM mechanism is a framework introduced to explain the suppression observed in FCNC decays. A key characteristic is that FCNC decays cannot proceed via a tree-level process but rather involve the exchange of two W bosons. In the presence of only the up-quark the decay amplitude is given by

$$\mathcal{A}_u \propto \cos\theta_c \sin\theta_c. \tag{2}$$

Since θ_c is non-vanishing, theoretical predictions expected FCNC decays such as $K_L^0 \to \mu^+\mu^-$ to be enhanced whilst the amplitude for $K^0 - \bar{K^0}$ mixing should be zero. In order to account for this discrepancy, Sheldon Glashow alongside John Iliopoulos and Luciano Maiani postulated the existence of the charm quark. One with a charge of $\frac{+2}{3}e$ as well as a coupling to the s and d mass eigenstates in an orthogonal combination with the up quark. This is necessary in order to introduce additional amplitudes such that

$$\mathcal{A}_c \propto -\sin\theta_c \cos\theta_c. \tag{3}$$

A consideration of both final state amplitudes yields the decay rate

$$|\mathcal{A}|^2 \propto |\mathcal{A}_u + \mathcal{A}_c|^2 \tag{4}$$

which contains mass dependent amplitudes, $\mathcal{A}_u$ and $\mathcal{A}_c$, that do not cancel completely due to a difference in mass between the up and charm quarks. As the decay rate is proportional to $m_c^2 - m_u^2$, the GIM mechanism could be used to predicted the mass of the charm quark to be $\sim 3\text{GeV/c}^2$ [35, 36].

2.3.2 The CKM matrix

The Cabibbo-Kobayashi-Maskawa (CKM) mechanism provides the theoretical description for CP-violation [37]. The interactions between charged currents and quarks are encoded in the following Lagrangian term:

$$\mathcal{L} = -\frac{g_w}{\sqrt{2}} \left[\bar{u} \gamma^\mu W_\mu^+ V_{CKM} d \right], \tag{5}$$

where g_w is the weak coupling constant, u are the three generations of up-type quark mass eigenstates, γ^μ are the Gamma matrices and W_μ^+ represents the W^+ boson. As such, weak interactions govern the flavour changing of up-type quarks, u, to down-type quarks, d. The weak eigenstates, d', can be thought of as a rotation of the mass eigenstates, d, given by the elements of the CKM matrix (V_{CKM}),

$$\begin{bmatrix} d' \\ s' \\ b' \end{bmatrix} = V_{CKM} \begin{bmatrix} d \\ s \\ b \end{bmatrix} = \begin{bmatrix} V_{ud} & V_{us} & V_{ub} \\ V_{cd} & V_{cs} & V_{cb} \\ V_{td} & V_{ts} & V_{td} \end{bmatrix} \begin{bmatrix} d \\ s \\ b \end{bmatrix}. \tag{6}$$

where V_{CKM} is an extension of the Cabibbo hypothesis to include a third generation of quarks. In addition, the matrix must be unitary since physics observations are independent of the choice of representation. For mass, $|\psi\rangle$, and flavour, $|\psi'\rangle$, eigenstates this means that

$$\langle \psi' | \psi' \rangle = \langle \psi | \psi \rangle = \langle \psi | \, V_{CKM}^\dagger V_{CKM} \, | \psi \rangle \,, \tag{7}$$

where $V_{CKM}^\dagger$ is the hermitian adjoint of V_{CKM} and $V_{CKM}^\dagger V_{CKM} = \mathbb{I}_3$. Here $\mathbb{I}_3$ is the three dimensional identity matrix and elements of V_{CKM} satisfy

$$\sum_{k=u,c,t} V_{ki}^* V_{kj} = \delta_{ij}. \tag{8}$$

An $N \times N$ matrix has $2N^2$ degrees of freedom. Due to the unitarity constraint, this number is reduced to N^2. In particular, $2N-1$ of these are not physically significant since a common phase can be absorbed into each quark field (both of the mass eigenstates, and of the weak eigenstates), making the matrix independent of this global phase. This leaves $(N-1)^2$ independent parameters. These comprise $\frac{1}{2}N(N-1)$ quark mixing angles and $\frac{1}{2}(N-1)(N-2)$ CP-violating complex phases. Thus the CKM matrix can be fully specified using four parameters; three quark mixing angles, θ_{12}, θ_{23}, θ_{13} as well as a single complex phase, δ_{CP}. This irreducible complex phase ensures that $V_{CKM}^\dagger \neq V_{CKM}$ and accounts for CP-violation in the SM. In the standard representation, the CKM matrix is written as follows

$$V_{CKM} = \begin{bmatrix} c_{12}c_{13} & s_{12}c_{13} & s_{13}e^{-i\delta_{CP}} \\ -s_{12}c_{23} - c_{12}s_{23}s_{13}e^{i\delta_{CP}} & c_{12}c_{23} - s_{12}s_{23}s_{13}e^{i\delta_{CP}} & s_{23}c_{13} \\ s_{12}c_{23} - c_{12}c_{23}s_{13}e^{i\delta_{CP}} & -c_{12}s_{23} - s_{12}c_{23}s_{13}e^{i\delta_{CP}} & c_{23}c_{13} \end{bmatrix}, \tag{9}$$

where the sine and cosine of the quark mixing angles are given by $s_{ij} = \sin\theta_{ij}$ and $c_{ij} = \cos\theta_{ij}$. Experimentally it has been determined that $s_{13} \ll s_{23} \ll s_{12} \ll 1$, thus the

largest elements reside on the leading diagonal. With this hierarchy in mind, four new parameters can be introduced such that

$$\begin{aligned} s_{12} &= \lambda = |V_{us}|^2 \approx 0.23, \\ s_{23} &= A\lambda^2, \\ s_{13}e^{-i\delta_{cp}} &= A\lambda^3(\rho - i\eta). \end{aligned} \tag{10}$$

In the Wolfenstein parameterisation [38] the CKM matrix becomes

$$V_{CKM} = \begin{bmatrix} 1 - \frac{\lambda^2}{2} & \lambda & A\lambda^3(\rho - i\eta) \\ -\lambda & 1 - \frac{\lambda^2}{2} & A\lambda^2 \\ A\lambda^3(1 - \rho - i\eta) & -A\lambda^2 & 1 \end{bmatrix} + \mathcal{O}\big(\lambda^4\big). \tag{11}$$

In this case CP-violation is described by a complex plane in $\bar{\rho}$ and $\bar{\eta}$ where $\bar{\rho} = \rho(1 - \lambda^2/2 + ...)$ and $\bar{\eta} = \eta(1 - \lambda^2/2 + ...)$. The observation of CP-violating effects necessitates that η differs from zero. It is evident that the matrix elements depend on powers of λ and govern the likelihood of observed transitions. As a result, transitions of quark flavour within the same generation are favoured whilst transitions between generations are suppressed, with the transition from the first to the third generation being the most suppressed. Since only the V_{ub} and V_{td} elements incorporate a complex phase up to $\mathcal{O}(\lambda^3)$, CP-violation in D mesons is expected to be negligible as $\mathcal{O}(\lambda^4)$ terms and higher are required.

The Wolfenstein parameterisation allows for a visualisation of the CKM matrix. By considering unitary requirements, the elements of V_{CKM} obey six vanishing constraints. One such relation is given by

$$V_{ub}^* V_{ud} + V_{cb}^* V_{cd} + V_{tb}^* V_{td} = 0 \tag{12}$$

where each term represents the side of a triangle in the complex plane, known as the unitarity triangle. The vertices of the unitarity triangle are $(0, 0)$, $(1, 0)$ and $(\bar{\rho}, \bar{\eta})$, whilst the angles are defined as

$$\begin{aligned} \alpha &= \arg\Big[-\frac{V_{tb}^* V_{td}}{V_{ub}^* V_{ud}}\Big], \\ \beta &= \arg\Big[-\frac{V_{cb}^* V_{cd}}{V_{tb}^* V_{td}}\Big], \\ \gamma &= \arg\Big[-\frac{V_{ub}^* V_{ud}}{V_{cb}^* V_{cd}}\Big]. \end{aligned} \tag{13}$$

A schematic representation of the unitarity triangle is shown in Fig. 3. The independent measurement of each angle provides a way to test the SM. In particular, the angle γ is of interest as only $b \to c$ and $b \to u$ transitions contribute at tree-level. Although these processes provide a clean environment, current experimental precision is statistically limited. These measurements require many final states in order to reduce statistical uncertainties.

The angle γ can be measured indirectly using global fits to the unitarity triangle under the assumption that it is closed. By measuring α and β, as well as the lengths of

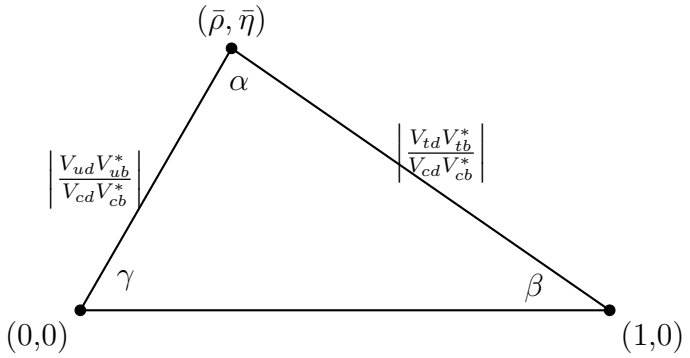


Figure 3: A schematic of the unitarity triangle.

the sides of the triangle, a value for γ can be inferred. Deviations from direct measurements could arise due to the presence of new physics since loop processes contribute to α and β. A recent combination published by LHCb yields $\gamma = (63.8^{+3.5}_{-3.7})^\circ$ [39] whilst indirect measurements suggest $\gamma = (65.5^{+1.1}_{-2.7})^\circ$ [40]. Currently, both measurements are in agreement.

2.4 Neutral meson mixing

Due to the noncoincidence of flavour and mass eigenstates, neutral mesons exhibit the phenomenon of mixing in which a particle can oscillate into the corresponding anti-particle. Such an observation has been made for each of the neutral mesons: K^0, B^0, B_s^0 and the D^0. The quantum state of a neutral meson, produced at $t = 0$, can be expressed as a superposition of the particle flavour eigenstates, D^0, and the anti-particle flavour eigenstates, $\bar{D}^0$, such that

$$|\psi\rangle = a(0)\left|D^0\right\rangle + b(0)\left|\bar{D}^0\right\rangle. \tag{14}$$

With time, the original quantum state will evolve according to

$$|\psi\rangle = a(t)\left|D^0\right\rangle + b(t)\left|\bar{D}^0\right\rangle \tag{15}$$

where $a(t)$ and $b(t)$ are normalised coefficients. The flavour conserving strong and electromagnetic interactions can be ignored. By applying the Weisskopf-Wigner approximation [41], the time evolution follows the Schrödinger equation

$$i\frac{\partial}{\partial t}|\psi(t)\rangle = \mathcal{H}|\psi(t)\rangle, \tag{16}$$

where $\mathcal{H}$ is the effective hamiltonian and combines two terms. Firstly a hermitian mass matrix, M, and an anti-hermitian decay matrix Γ. It is the non-zero diagonal elements of $\mathcal{H}$ that result in mixing. The effective hamiltonian has the form

$$\mathcal{H} = M - i\frac{\Gamma}{2} = \begin{pmatrix} M_{11} - i\frac{\Gamma_{11}}{2} & M_{12} - i\frac{\Gamma_{12}}{2} \\ M_{21} - i\frac{\Gamma_{21}}{2} & M_{22} - i\frac{\Gamma_{22}}{2} \end{pmatrix} = \begin{pmatrix} M_{11} - i\frac{\Gamma_{11}}{2} & M_{12} - i\frac{\Gamma_{12}}{2} \\ M_{12}^* - i\frac{\Gamma_{12}^*}{2} & M_{22} - i\frac{\Gamma_{22}}{2} \end{pmatrix} \tag{17}$$

Virtual intermediate states, which are off-shell contributions, are contained within elements of M, whilst on-shell contributions are specified by Γ. By substituting Eq.17 into Eq.16, the mass eigenstates $|D_1\rangle$ and $|D_2\rangle$ can be related to the flavour eigenstates

$$\begin{aligned} |D_1\rangle &= p\left|D^0\right\rangle + q\left|\bar{D}^0\right\rangle \\ |D_2\rangle &= p\left|D^0\right\rangle - q\left|\bar{D}^0\right\rangle, \end{aligned} \tag{18}$$

where p and q are complex numbers that satisfy $|p|^2 + |q|^2 = 1$ and

$$\left(\frac{q}{p}\right)^2 = \frac{M_{12}^* - i\Gamma_{12}^*}{M_{12} - i\Gamma_{12}}. \tag{19}$$

In the limit of CP symmetry the $|D_1\rangle$ state is CP-even whilst $|D_2\rangle$ is CP-odd. As $|D_{1,2}\rangle$ are eigenstates of $\mathcal{H}$, solving Eq.16 yields

$$|D_{1,2}\rangle = e^{-im_{1,2}t - \frac{1}{2}\Gamma_{1,2}t}\,|D_{1,2}(0)\rangle\,. \tag{20}$$

By re-arranging Eq.18 the following expressions for the flavour eigenstates are obtained

$$\begin{aligned} \left|D^0\right\rangle &= \frac{1}{2p}(|D_1\rangle + |D_2\rangle) \\ \left|\bar{D}^0\right\rangle &= \frac{1}{2q}(|D_1\rangle - |D_2\rangle). \end{aligned} \tag{21}$$

Substituting Eq.20 into Eq.21 and using Eq.18, the time dependence of flavour eigenstates emerges

$$\begin{aligned} \left|D^0(t)\right\rangle &= g_+(t)\left|D^0\right\rangle + \frac{q}{p}g_-(t)\left|\bar{D}^0\right\rangle, \\ \left|\bar{D}^0(t)\right\rangle &= \frac{p}{q}g_-(t)\left|D^0\right\rangle + g_+(t)\left|\bar{D}^0\right\rangle \end{aligned} \tag{22}$$

where

$$\begin{aligned} g_\pm(t) &= \frac{e^{-i\lambda_1 t} \pm e^{-i\lambda_2 t}}{2}, \\ \lambda_{1,2} &= M - \frac{i\Gamma}{2} \pm \frac{q}{p}\left(M_{12} - \frac{i\Gamma_{12}}{2}\right). \end{aligned} \tag{23}$$

In Eq.23 M is the average mass $\frac{m_1+m_2}{2}$ whilst Γ is the average lifetime $\frac{\Gamma_1+\Gamma_2}{2}$. The differences in mass, ΔM, and differences in width, $\Delta\Gamma$, are given by $m_1 - m_2$ and $\Gamma_1 - \Gamma_2$ respectively. The mixing probabilities are

$$\begin{aligned} \mathcal{P}(D^0(t) \to D^0) &= \mathcal{P}(\bar{D}^0(t) \to \bar{D}^0) \\ &= |g_+(t)|^2 \end{aligned} \tag{24}$$

$$\mathcal{P}(D^0(t) \to \bar{D}^0) = \left|\frac{q}{p}\right|^2 |g_-(t)|^2 \tag{25}$$

$$\mathcal{P}(\bar{D}^0(t) \to D^0) = \left|\frac{p}{q}\right|^2 |g_-(t)|^2 \tag{26}$$

The mixing equations show that the the probability of preserving initial flavour is identical for both the particle and anti-particle states whilst the mixing probability depends on

the initial state. In the limit of CP-symmetry, the mixing parameters are defined by normalised mass and decay-rate differences of the eigenstates [36]:

$$\begin{aligned} x &= \frac{m_1 - m_2}{\Gamma} = \frac{\Delta M}{\Gamma} \\ y &= \frac{\Gamma_1 - \Gamma_2}{2\Gamma} = \frac{\Delta \Gamma}{2\Gamma}. \end{aligned} \tag{27}$$

The mixing parameter x can be thought of as the number of meson anti-meson oscillations prior to decay whilst y governs the decay trend. The expressions for $|g_{\pm}(t)|^2$ can be expanded explicitly in terms of the mixing parameters:

$$|g_{\pm}(t)|^2 = \frac{e^{-\Gamma t}}{2}(\cosh(y\Gamma t) \pm \cos(x\Gamma t)). \tag{28}$$

Although the mixing formalism is identical for each of the neutral meson systems, the observed behaviour varies significantly. These discrepancies are a result of the interactions contributing to the M_{12} and Γ_{12} matrix elements. The x and y observeables, governing the oscillations in D^0, B^0, B_s^0 and K^0 systems are presented in Table 1.

Table 1: The experimental status of x and y for each of the neutral meson systems [42].

System	x	y
$K^0 - \bar{K}^0$	-0.946 ± 0.004	0.99650 ± 0.00001
$D^0 - \bar{D}^0$	$(0.407 \pm 0.044)\%$	$(0.647 \pm 0.024)\%$
$B^0 - \bar{B}^0$	0.769 ± 0.004	0.001 ± 0.01
$B_s^0 - \bar{B}_s^0$	27.03 ± 0.09	0.126 ± 0.007

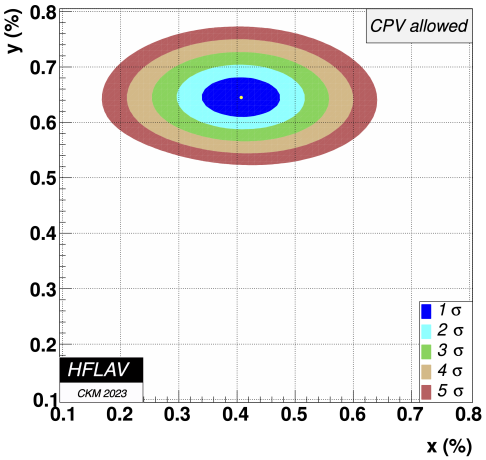


Figure 4: Current experimental status of the x and y charm mixing parameters [43].

By inspection of the mixing parameters it is evident that the B_s^0 system has the highest frequency of oscillations whilst the D^0 has by far the lowest. As the mass difference between the D_1 and D_2 eigenstates is very small, the number of oscillations prior to decay is also very small. In fact, only recent measurements at LHCb have observed this

mass difference to be non-zero [44]. Improving the knowledge of x and y in the charm is a motivation for this thesis with the current experimental status show in Fig. 4. For each of the meson systems Eq. 28 can be used to plot a visualisation of the oscillatory behaviour, as presented in Fig. 5.

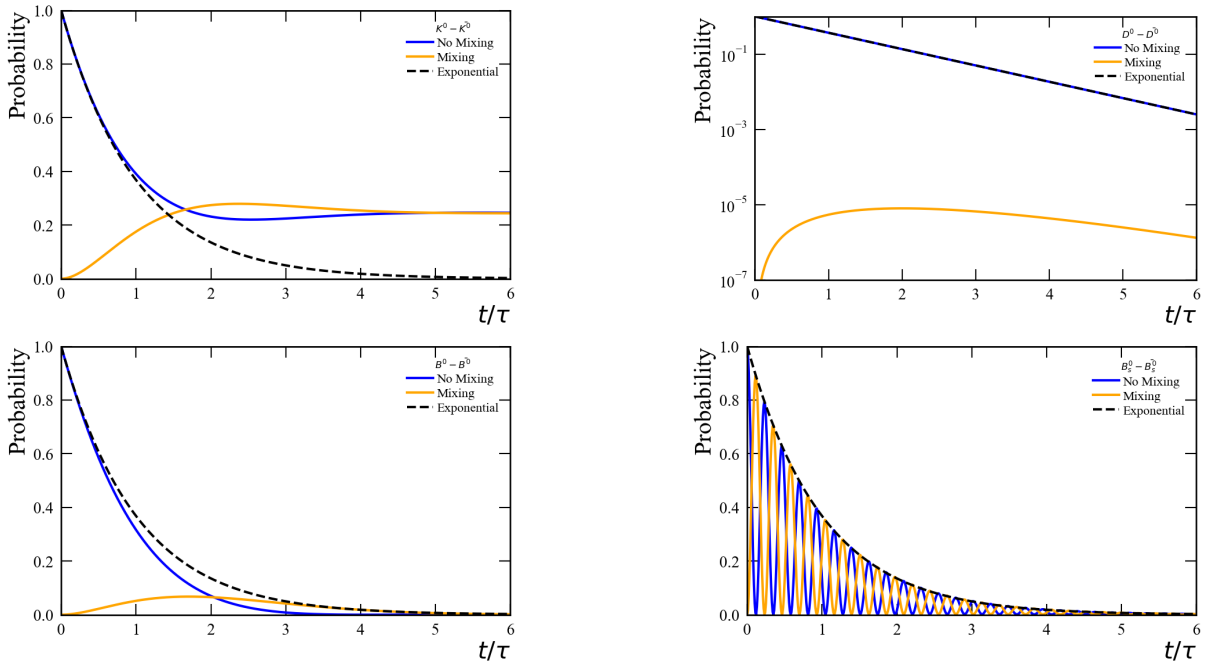


Figure 5: Plots showing oscillations for neutral mesons as a function of time, assuming $\left|\frac{q}{p}\right| = 1$. The exponential function corresponds to $x = y = 0$. For the $D^0 - \bar{D}^0$ system the probability is shown on a logarithmic scale. Oscillations are shown for the K^0 (top left), D^0 (top right), B^0 (bottom left) and B_S^0 (bottom right) systems. The population of neutral mesons is unmixed.

There exist two categories of amplitudes which contribute to mixing. The first are short-range interactions that proceed via box diagrams. An example is shown in Fig. 2. In such a scenario a virtual quark is exchanged. This is an off-shell interaction involving W bosons and heavy quarks. For the D^0 meson, the dominant contribution involves the exchange of the b quark. The second amplitude arises due to long-distance scattering. This process is characterised by the exchange of on-shell hadrons. Specifically, a neutral meson decaying into a common final state which then recombines into the corresponding neutral anti-meson. The contribution of this scatting amplitude is proportional to the phase-space shared by the neutral meson and its antiparticle. In the case of the D^0, the short-range interactions are suppressed by the GIM mechanism, and therefore it is the long-distance scattering effects that dominate.

2.5 Classification of CP-violation

Although the neutral mixing phenomenon incorporates CP-violation, such an effect can be observed in direct decays to a generic final state f. The corresponding decay ampli-

tudes are given by

$$\begin{aligned} \mathcal{A}_f &= \langle f | \mathcal{H} \left| D^0 \right\rangle, \;\; \mathcal{A}_{\bar{f}} = \left\langle \bar{f} \right| \mathcal{H} \left| D^0 \right\rangle, \\ \bar{\mathcal{A}}_f &= \langle f | \mathcal{H} \left| \bar{D}^0 \right\rangle, \;\; \bar{\mathcal{A}}_{\bar{f}} = \left\langle \bar{f} \right| \mathcal{H} \left| \bar{D}^0 \right\rangle. \end{aligned} \tag{29}$$

The expressions for these amplitudes can be expanded as a series of all possible contributions

$$\begin{aligned} \mathcal{A}_f &= \sum_n \left|\mathcal{A}_f^n\right| e^{i\delta_f^n} e^{i\phi_f^n}, \\ \bar{\mathcal{A}}_{\bar{f}} &= \sum_n \left|\mathcal{A}_f^n\right| e^{i\delta_f^n} e^{-i\bar{\phi_f^n}}, \end{aligned} \tag{30}$$

where $\left|\mathcal{A}_f^n\right|$ is the magnitude of the decay amplitude for a process at order n. The elements δ_f^n are the strong phases and arise due to strong interactions in the hadronic system. The strong phases remain invariant under a CP transformation. The elements ϕ_f^k are the weak phases related to the complex phase in the CKM matrix and crucially change sign under CP conjugation. In processes that involve decays of neutral mesons there exist three contributing mechanisms; CP-violation in decay, CP-violation in mixing as well as CP-violation due to the inference between decay and mixing.

2.5.1 CP-violation in the decay

The phenomenon of CP-violation in the decay arises due to a difference in decay widths between particles and anti-particles. The CP asymmetry for a meson decaying to a self conjugate final state is defined as

$$\begin{aligned} A_{CP} &= \frac{\left|\Gamma(D^0 \to f)\right|^2 - \left|\Gamma(\bar{D}^0 \to \bar{f})\right|^2}{\left|\Gamma(D^0 \to f)\right|^2 + \left|\Gamma(\bar{D}^0 \to \bar{f})\right|^2} \\ &= -\frac{2\sum_{nm} \left|\mathcal{A}_f^n\right| \left|\mathcal{A}_f^m\right| \sin\left(\delta_f^n - \delta_f^m\right) \sin\left(\phi_f^n - \phi_f^m\right)}{\sum_{nm} \left|\mathcal{A}_f^n\right|^2 + \left|\mathcal{A}_f^m\right|^2 + 2\left|\mathcal{A}_f^n\right| \left|\mathcal{A}_f^m\right| \cos\left(\delta_f^n - \delta_f^m\right) \cos\left(\phi_f^n - \phi_f^m\right)}. \end{aligned} \tag{31}$$

In order for CP-violation to occur there must exist at least two contributing processes with a non vanishing weak and strong phase difference. Both charged and neutral meson decays are sensitive to this type of CP-violation under the condition:

$$\left|\mathcal{A}(D^0 \to f)\right| \neq \left|\mathcal{A}(\bar{D}^0 \to \bar{f})\right| \tag{32}$$

which ensures that A_{CP} differs from zero. In the charm sector, CP-violation in the decay has only recently been observed by the LHCb collaboration [45].

2.5.2 CP-violation in mixing

The phenomenon of CP-violation in mixing occurs due to a difference in mixing probabilities between particles and anti-particles. The condition for this type of CP-violation is such that:

$$\mathcal{P}(D^0 \to \bar{D}^0) \neq \mathcal{P}(\bar{D}^0 \to D^0). \tag{33}$$

To satisfy this condition it follows that $\left|\frac{q}{p}\right| \neq 1$. In the charm system the SM predicts CP-violation in mixing to be very small but could be enhanced by new physics phenomena.

2.5.3 CP-violation due to the interference between decay and mixing

The final mechanism for CP-violation is due to the interference between decay and mixing amplitudes. In order for this type of CP-violation to occur, the final states must be accessible by both the particle and the corresponding anti-particle such that the $D^0 \to f$ decay interferes with a $D^0 \to \bar{D}^0 \to f$ process. This is characterised by a complex phase, λ_f, defined as

$$\lambda_f = \frac{q}{p}\frac{\bar{\mathcal{A}}_f}{\mathcal{A}_f}. \tag{34}$$

In the instance that $\arg(\lambda_f)$ differs from zero, this type of CP-violation will occur. Therefore improving measurements of charm mixing parameters will help in the search for CP-violation in the charm system in mixing as well as in the interference between decay and mixing.

2.6 Self conjugate multi-body final states

When analysing the decays of particles into multi-body final states, the phase-space of the system is characterised by kinematic degrees of freedom. In the case of a particle with mass M decaying into three final-state particles with masses m_1, m_2 and m_3, each represented by a momentum four-vector, there are a total of twelve kinematic parameters. Due to constraints imposed by the conservation of four-momentum, the number of free parameters is reduced to eight. For an isotropic decay, one involving a pseudo-scalar meson, the orientation of the decay is described by three Euler angles thus reducing the available degrees of freedom to five. Lastly, each decay product is required to have an on-shell mass reducing the available degrees of freedom down to two. A common choice involves the combinations of squares of invariant masses of the final-state particles m^2_{12} and m^2_{23} such that

$$m^2_{ij} = (E_i + E_j)^2 - |\vec{p_i} + \vec{p_j}|^2, \tag{35}$$

where E are the energies and $\vec{p}$ are the three momenta of the particles.

The decay phase-space of a three body final state can be visualised on a 'Dalitz plot' as shown in Fig. 6, the boundaries of which are determined by kinematic constraints such that:

$$m^2_{12} + m^2_{13} + m^2_{23} = M^2 + m^2_1 + m^2_2 + m^2_3. \tag{36}$$

A decay process proceeding directly to the final state will produce a uniform distribution across the Dalitz plane. Observed horizontal, vertical and diagonal bands correspond to resonant structures which are short-lived intermediate states that subsequently decay into lighter particles. The density distribution along a band is governed by the spin of the resonance. The "Dalitz plot" is useful when searching for new resonances such as exotic mesons or when searching for asymmetry between matter and anti-matter.

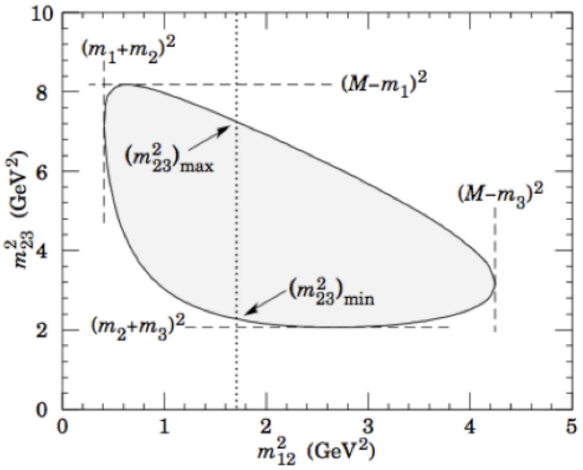


Figure 6: Example of a Dalitz plot for a three body final state [46].

2.7 Measuring charm mixing parameters with the bin-flip method

This analysis attempts to measure charm mixing parameters by applying a model independent approach known as the bin-flip method to the $D^0 \to K^0_S K^+ K^-$ decay mode for the first time at LHCb. In this analysis, the Dalitz plane is partitioned into regions according to the "iso-$\Delta\delta$" binning scheme as shown in Fig. 7. This thesis focuses solely on the $\mathcal{N} = 2$ scenario. The boundaries of these regions were originally optimised by

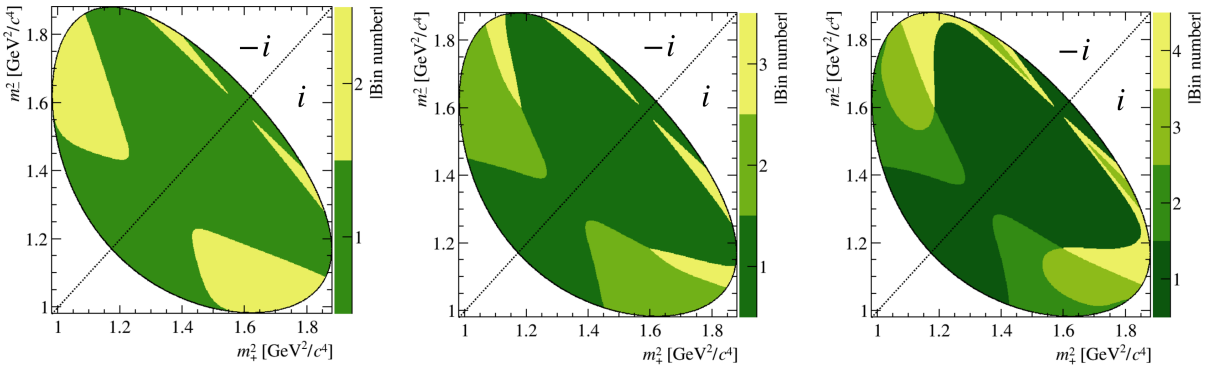


Figure 7: Division of the $D^0 \to K^0_S K^+ K^-$ Dalitz plane into $\mathcal{N} = 2, 3$ and 4 bins [21]. The sloped black line corresponds to the principal bisector, region where $m^2_+ = m^2_-$. Bins above the principal bisector are labeled with a negative bin index, $-i$, whilst bins below the principal bisector are labeled with a positive bin index, i.

the CLEO collaboration [21] and applied to a measurement of the CKM angle γ. These boundaries are created by partitioning the Dalitz plane into a semispace of $\mathcal{N}$ bins under the condition

$$2\pi\frac{(i-\frac{3}{2})}{\mathcal{N}} < \Delta\delta < 2\pi\frac{(i-\frac{1}{2})}{\mathcal{N}}, \text{ for } b = i, ..., \mathcal{N} \tag{37}$$

which aims to preserve an approximately constant strong-phase difference in each Dalitz bin, according to the expectations of an amplitude model. For a self-conjugate multi-body final state there exists a strong phase difference, $\Delta\delta$, between the D^0 and $\bar{D}^0$ mesons which varies over the "Dalitz plot". Within each Dalitz bin i, $c_i = \cos(\Delta\delta)$ whilst $s_i = \sin(\Delta\delta)$

and parameterise the interference between the D^0 and $\bar{D}^0$ decay amplitudes. In order to produce the "Dalitz plot", the dynamics of a three body decay, $D^0 \to K^0_S K^+ K^-$, can be fully specified using a pair of flavour dependent-invariant masses, $m^2_\pm$. Following the Dalitz formalism [47, 48]:

$$m^2_\pm = \begin{cases} m^2(K^0_S K^\pm), & \text{for } D^0 \to K^0_S K^+ K^- \\ m^2(K^0_S K^\mp), & \text{for } \bar{D}^0 \to K^0_S K^+ K^-. \end{cases} \tag{38}$$

The bin-flip method is an approach which enables mixing and CP-violating parameters to be measured in a model-independent manner. Ratios of self-conjugate decays are considered in kinematically similar regions, obviating the need for an accurate description of acceptance effects. The decay phase-space or "Dalitz plot" is partitioned into regions (bins) which are symmetric about the principal bisector, a line corresponding to $m^2(K^0_S K^+)$ $(m^2_+) = m^2(K^0_S K^-)$ (m^2_-). A positive bin label is assigned in the lower region, $m^2_+ > m^2_-$, and a negative bin label in the upper region, $m^2_+ < m^2_-$. The Dalitz bins are defined such that the variation of the strong phase difference across each bin is approximately constant. Ratios of observed signal yields on opposite sides of the principal bisector are calculated as a function of the D^0 decay-time. The time-dependent values of these ratios are governed by charm-mixing and CP-violating parameters which are extracted using a least-squares fit.

2.7.1 Formalism

The amplitude for a decay to a final sate, $f = K^0_S K^+ K^-$, varies with position in phase-space. In the limit of CP symmetry, $A_f(m^2_+, m^2_-) = \bar{A}_f(m^2_-, m^2_+)$ where A_f and $\bar{A}_f$ are the D^0 and $\bar{D}^0$ amplitudes to the same final state, f. The time evolution satisfies

$$\left|\mathcal{A}(m^2_+, m^2_-; t)\right|^2 = \left| A_f(m^2_+, m^2_-) g_+(t) + \bar{A}_f(m^2_-, m^2_+) \frac{q}{p} g_-(t) \right|^2 \text{ and} \tag{39}$$

$$\left|\bar{\mathcal{A}}(m^2_+, m^2_-; t)\right|^2 = \left| \bar{A}_f(m^2_+, m^2_-) g_+(t) + A_f(m^2_-, m^2_+) \frac{p}{q} g_-(t) \right|^2, \tag{40}$$

where $g_\pm(t) = \theta(t) e^{-imt} e^{\frac{-t}{2}} \begin{matrix}\cosh \\ \sinh\end{matrix}(\frac{zt}{2})$, t is the life-time in units of the D^0 decay-time, m is the average mass, $\theta(t)$ is the Heaviside step function and z is defined as $-(y + ix)$. The total number of mesons in Dalitz bin i, $N_i(t)$, at given time t, can be obtained using:

$$\begin{aligned} N_i(t) &= \int_i dm^2_+ dm^2_- \left|\mathcal{A}(m^2_+, m^2_-; t)\right|^2 \\ &= F_i |g_+(t)|^2 + \left|\frac{q}{p}\right|^2 \bar{F}_{-i} |g_-(t)|^2 + 2\sqrt{\bar{F}_{-i} F_i}\, \mathrm{Re}\left[\frac{q}{p} X_i g^\dagger_+(t) g_-(t)\right] \end{aligned} \tag{41}$$

and similarly for antimesons, $\bar{N}_i(t)$, with $\mathcal{A}(m^2_+, m^2_-; t) \leftrightarrow \bar{\mathcal{A}}(m^2_+, m^2_-; t)$. In the above expression, F_i $(\bar{F}_i)$ correspond to fractional yields of D^0 $(\bar{D}^0)$ mesons in a Dalitz bin i at $t = 0$ and can be calculated using:

$$F_i = \int_i dm^2_+ dm^2_- \left|A_f(m^2_+, m^2_-)\right|^2, \;\; \bar{F}_i = \int_i dm^2_+ dm^2_- \left|\bar{A}_f(m^2_+, m^2_-)\right|^2, \tag{42}$$

$$X_i = \frac{1}{\sqrt{F_i \bar{F}_{-i}}} \int_i dm_+^2 dm_-^2 A_f^\dagger(m_+^2, m_-^2) \bar{A}_f(m_-^2, m_+^2), \tag{43}$$

where X_i is a an interference term such that $|X_i| \leq 1$ and $X_{-i} = X_i^\dagger$. CP-conservation in the decay implies $A_f = \bar{A}_f$, $\bar{F}_i = F_i$ and $\bar{X}_i = X_i$. As such, the interference term $X_i = c_i - is_i$ can be separated into real and imaginary components:

$$c_i = \frac{1}{\sqrt{F_i F_{-i}}} \int_i dm_+^2 dm_-^2 \big|A_f(m_+^2, m_-^2)\big|\big|A_f(m_-^2, m_+^2)\big| \cos\left(\Delta\delta(m_+^2, m_-^2)\right) \text{ and} \tag{44}$$

$$s_i = \frac{1}{\sqrt{F_i F_{-i}}} \int_i dm_+^2 dm_-^2 \big|A_f(m_+^2, m_-^2)\big|\big|A_f(m_-^2, m_+^2)\big| \sin\left(\Delta\delta(m_+^2, m_-^2)\right), \tag{45}$$

where $\delta(m_+^2, m_-^2)$ is the strong phase of $A_f(m_+^2, m_-^2)$ and $\Delta\delta(m_+^2, m_-^2)$ is given by $\delta(m_+^2, m_-^2) - \delta(m_-^2, m_+^2)$. Hence, c_i and s_i are the amplitude-weighted cosine and sine of the strong phase difference within Dalitz bin i. A nonuniform variation in selection and reconstruction efficiencies, $\epsilon(m_+^2, m_-^2)$, across the Dalitz plane leads to a modification of F_i, $\bar{F}_i$ and X_i. An experimental efficiency which varies symmetrically about the principal bisector is advantageous as both F_i and $\bar{F}_i$ are similarly affected, leaving X_i unchanged. Mixing parameters are known to be small, allowing for the expansion:

$$|g_+(t)|^2 \approx e^{-t} + \frac{1}{4} e^{-t} t^2 \,\mathrm{Re}(z^2) + \mathcal{O}\big(z^4\big), \tag{46}$$

$$|g_-(t)|^2 \approx \frac{1}{4} e^{-t} t^2 |z|^2 + \mathcal{O}\big(z^4\big) \text{ and} \tag{47}$$

$$g_+^\dagger(t) g_-(t) \approx \frac{1}{2} e^{-t} t z + \mathcal{O}\big(z^3\big). \tag{48}$$

The summation of the above relations over a given decay time bin j yields:

$$\int_i |g_+|(t) dt \approx C[1 + \frac{1}{4} \langle t^2 \rangle_i \,\mathrm{Re}(z^2)], \tag{49}$$

$$\int_i |g_-|(t) dt \approx \frac{C_i}{4} \langle t^2 \rangle_i \,\mathrm{Re}(z^2), \tag{50}$$

$$\int_i g_+^\dagger(t) g_-(t) dt \approx \frac{C_i}{2} \langle t \rangle_i z, \tag{51}$$

where $\langle ... \rangle_j$ is the expectation value of the exponential distribution in a decay time bin j and C_j is the normalisation. If the variation of the decay-time acceptance efficiency, $\epsilon(t)$, is nonuniform across a decay-time bin, the expectation value is calculated using the observed distribution of unmixed mesons, $\epsilon(t) e^{-t}$. The dependence of the bin-flip method on decay-time acceptance efficiency is minimal and does not require a detailed knowledge of the Dalitz acceptance.

The total number of a neutral D mesons initially produced in the D^0 flavour eigenstate in a decay-time bin j and Dalitz bin i can be obtained using:

$$\begin{aligned} N_{ij} &= \int_j N_i(t) dt \\ &\approx F_i[1 + \frac{1}{4} \langle t^2 \rangle_j \,\mathrm{Re}(z^2)] + \frac{1}{4} \langle t^2 \rangle_j |z|^2 \left|\frac{q}{p}\right|^2 F_{-i} + \langle t \rangle_j \sqrt{F_{-i} F_i} \,\mathrm{Re}\left(\frac{q}{p} X_i z\right), \end{aligned} \tag{52}$$

where the normalisation constant has been omitted. Thus, the ratio of yields of D^0 mesons in Dalitz bin $-i$ and Dalitz bin i, for a given decay-time bin j, is given by:

$$\begin{aligned} R_{ij} &= \frac{N_{-ij}}{N_{ij}} \\ &\approx \frac{r_i[1 + \frac{1}{4}\langle t^2\rangle_j \,\mathrm{Re}(z^2)] + \frac{1}{4}\langle t^2\rangle_j |z|^2 \left|\frac{q}{p}\right|^2 + \langle t\rangle_j \sqrt{r_i}\,\mathrm{Re}\left(\frac{q}{p} X_i^\dagger z\right)}{1 + \frac{1}{4}\langle t^2\rangle_i \,\mathrm{Re}(z^2) + \frac{1}{4}\langle t^2\rangle_j |z|^2 r_i \left|\frac{q}{p}\right|^2 + \langle t\rangle_j \sqrt{r_i}\,\mathrm{Re}\left(\frac{q}{p} X_i z\right)} \end{aligned} \tag{53}$$

where r_i is defined as $\frac{F_{-i}}{F_i}$. By substituting $\frac{q}{p} \leftrightarrow \frac{p}{q}$ in equations 52 and 53, the yields, $\bar{N}_{ij}$, and ratios, $\bar{R}_{ij}$, for a neutral D meson initially produced in the $\bar{D}^0$ flavour eigenstate are obtained. Ultimately, mixing and CP-violating parameters are extracted using a χ^2 fit of the ratios R_{ij} and $\bar{R}_{ij}$. In addition, hadronic parameters c_i and s_i, are constrained using independent auxiliary inputs obtained from the BESIII experiment [22].

In practice, the bin-flip method can be prone to fit instabilities caused by terms such as $(\frac{q}{p})^{\pm 1} z$ which suffer from a degradation in sensitivity when $|z| \approx 0$. To control the fit stability, the fit parameters are redefined:

$$z_{CP} \pm \Delta z = (\frac{q}{p})^{\pm 1} z \rightarrow z^2 = z_{CP}^2 - \Delta z^2, \tag{54}$$

where $(\frac{q}{p})^2 = \frac{z_{CP}+\Delta z}{z_{CP}-\Delta z}$. Consequently, by defining $R_{ij} = R_{ij}^+$,$\bar{R}_{ij} = R_{ij}^-$ the ratios become

$$R_{ij}^{\pm} \approx \frac{r_i[1 + \frac{1}{4}\langle t^2\rangle_j \,\mathrm{Re}(z_{CP}^2 - \Delta z^2)] + \frac{1}{4}\langle t^2\rangle_j |z_{CP} \pm \Delta z|^2 + \langle t\rangle_j \sqrt{r_i}\,\mathrm{Re}(X_i^\dagger (z_{CP} \pm \Delta z))}{1 + \frac{1}{4}\langle t^2\rangle_j \,\mathrm{Re}(z_{CP}^2 - \Delta z^2) + r_i \frac{1}{4}\langle t^2\rangle_j |z_{CP} \pm \Delta z|^2 + \langle t\rangle_j \sqrt{r_i}\,\mathrm{Re}(X_i (z_{CP} \pm \Delta z))}. \tag{55}$$

The components of z_{CP} can be interpreted as the CP averaged mixing parameters $x_{CP} = -\,\mathrm{Im}(z_{CP})$ and $y_{CP} = -\,\mathrm{Re}(z_{CP})$, whilst the components of Δz can be interpreted as the CP-violating differences $\Delta x = -\,\mathrm{Im}(\Delta z)$ and $\Delta y = -\,\mathrm{Re}(\Delta z)$ [49, 50]. In the final fit the parameters c_i and s_i are all externally constrained. Additionally the term $z_{CP} \pm \Delta z$ has four parameters, however Δx and Δy are fixed to zero. Since this analysis focuses on two Dalitz bin scheme, at least two decay-time bins are required in order to perform the measurement.

2.8 Quantum-correlated $D\bar{D}$ decays

In this analysis, auxiliary information on the hadronic parameters c_i and s_i is used to constrain the model independent approach, the values of which are taken from a recent combination of CLEO-c and BESIII measurements [51, 52]. The CLEO-c and BESIII experiments are known as charm factories which study e^+e^- collisions at the $\psi(3770)$ resonance, threshold for $c\bar{c}$ production. The $\psi(3770)$ resonance is a charge conjugation eigenstate with $C = -1$ and predominantly decays into a pair of $D\bar{D}$ mesons. Since there are no other decay products, the $D\bar{D}$ pair are produced in a state with a defined C quantum number that is conserved. This entangled state can be used to directly access strong phase information. Quantum correlation effects appear as an enhancement or a suppression of decay rates governed by the CP content of the D decays.

In order to extract strong phase information at charm factories, the decay phase-space is partitioned into bins according to a binning scheme. In this analysis the bin-flip method utilises an identical binning scheme to that of CELO-c and BESIII. By tagging the flavour or CP state of one of the D mesons, the flavour or CP state of the other meson becomes known due to the entanglement. For instance, by flavour tagging one of the D mesons in a Cabbibo-favoured $D^0 \to K^-\pi^+$ decay, the other meson can be reconstructed as $\bar{D}^0 \to K^0_S K^+ K^-$. Additionally, by instead tagging the CP eigenstate of $D_{CP+} \to K^+K^-$, the other meson can be reconstructed as $D_{CP-} \to K^0_S K^+ K^-$. Finally both of the mesosns can be reconstructed as $D \to K^0_S K^+ K^-$ leading to interference. For each of these methodologies the observed decay rate depends on the observed fractional yields and strong phases within each "Dalitz plot" bin. The values for c_i and s_i used to constrain the mixing fit in this analysis are presented in Table 2.

Table 2: The vales of c_i and s_i used to constrain the mixing fit. The first uncertainty is statistical and the second is systematic [51].

i	c_i	s_i
1	$0.704 \pm 0.034 \pm 0.003$	$0.038 \pm 0.144 \pm 0.039$
2	$0.760 \pm 0.040 \pm 0.007$	$0.590 \pm 0.198 \pm 0.085$

3 The Large Hadron Collider (LHC) and the LHCb experiment

3.1 The Large Hadron Collider (LHC)

The European Organisation for Nuclear Research (*Conseil europeen pour la recherche nucleaire*, CERN) is a laboratory that hosts the world's largest particle physics collider. The CERN accelerator complex is presented in Fig. 8. The LHC operates as follows. Protons are extracted by ionising hydrogen gas, accelerated from rest to 50 MeV by a linear accelerator (LINAC 2) and then to 1.4 GeV by the BOOSTER (Proton Synchroton Booster). At the next stage, the Proton Synchroton (PS) accelerates protons to 25 GeV, followed by the Super Proton Synchrotron (SPS) which accelerates these protons to 450 GeV. At this stage, the protons are injected into the LHC machine and circulate the 27 km ring in bunches of up to $\mathcal{O}(10^{11})$ protons for approximately 12 hours (a fill). During the circulation, quadrupole magnets focus the beam while dipole magnets bend the beams' trajectory. Radio frequency (RF) cavities boost the circulating beam to the desired energy. During a fill, beams propagating in opposite directions collide at a frequency of 40 MHz at four possible locations. These are the ATLAS, ALICE, CMS and LHCb detectors [54]. This thesis focuses on Run II (between 2016 and 2018), where the LHCb detector collected pp collision data at a center-of-mass energy of $\sqrt{s} = 13$ TeV and a corresponding integrated luminosity of 5.7 fb^{-1}.

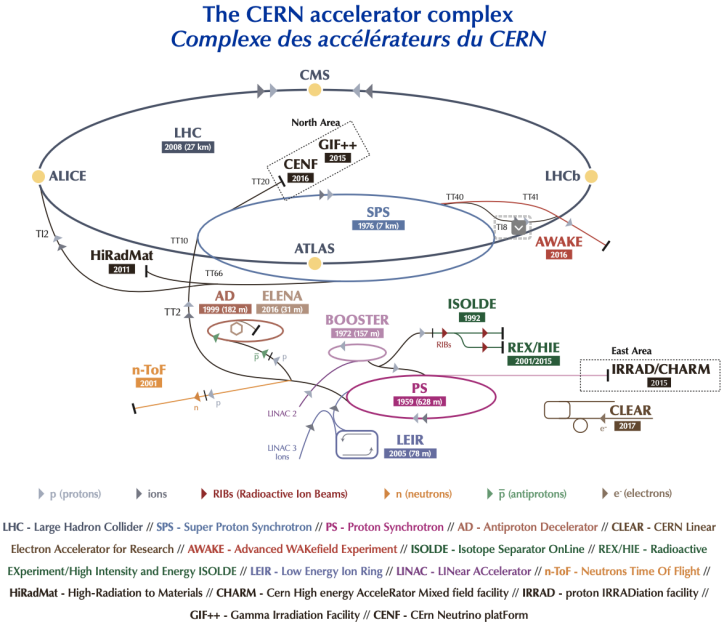


Figure 8: The CERN accelerator complex [53].

3.2 The LHCb detector

The LHCb experiment performs precision measurements within the field of flavour physics. In particular, the primary objectives involve searches for CP-violation and rare decays. The LHCb detector, shown in Fig. 9, was configured as a single-arm spectrometer with

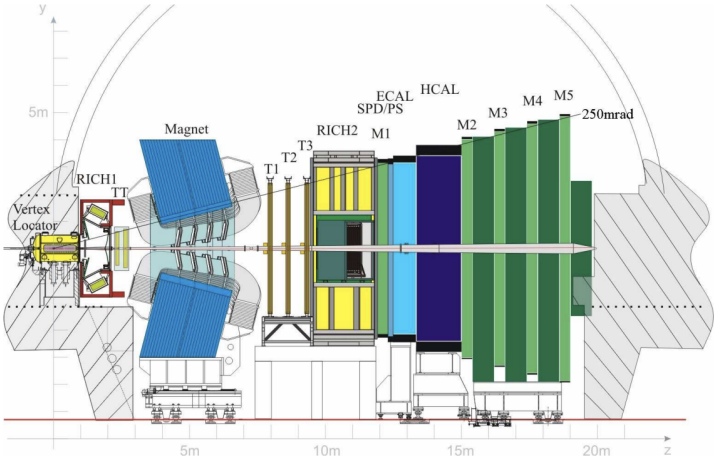


Figure 9: A schematic depicting the LHCb detector during Run II (2016-2018).

forward angular acceptance between approximately 10 mrad and 300 mrad (250 mrad) in the bending (non-bending) plane. This corresponds to a pseudorapidity range of $1.6 < \eta < 4.9$, where η is the angular coverage measured with respect to the beam axis such that $\eta = -\ln\left(\tan\left(\frac{\theta}{2}\right)\right)$. The geometry is optimised in order to maximise the detection of particles produced at very small angles relative to the beam pipe since the production cross sections of $c\bar{c}$ and $b\bar{b}$ hadrons peak in the forward and backward regions.

The Vertex Locator (VELO) is a large-area silicon strip detector surrounding the proton-proton, pp, collision point and is used to determine the location of primary vertices. Additionally the VELO allows for a determination of the displaced decay vertices of b and c-hadrons since the close arrangement of silicon strips ensures a precise spatial resolution. The first RICH (Ring Imaging Cherenkov) detector is located upstream of the magnet and assists in identifying low momentum particles whilst the second is downstream of the magnet and identifies particles with high momenta. The RICH detectors measure the Cherenkov radiation deposited by charged particles when propagating through a medium. Crucially, the observed emission angle is inversely proportional to the velocity of propagation. The magnet, with a bending power of approximately 4 Tm, deflects the trajectories of charged particles, to the left or to the right, in a direction perpendicular to the beam-pipe. As such, the radius of curvature is then used to calculate momenta, which combined with measurements of velocity yield the mass of the particle.

There are tracking systems stationed throughout the detector. Firstly Tracker Turicensis (TT) is a large area silicon strip detector located upstream of the magnet. The objective of the TT is to provide a measurement prior to deflection by the magnetic field. Downstream of the magnet there are three tracking stations (T1,T2,T3). Each comprises of an inner tracker (IT) and an outer tracker (OT). The inner trackers consist of silicon strips and covers the region closest to the beampipe. The outer trackers are made of straw drift tubes and cover the outer region. Hits recorded by the silicon strips are used to reconstruct trajectories. The calorimeter system is a combination of scintillating pads (SPD), preshower detectors (PS), electromagnetic (ECAL) as well as hadronic calorimeters (HCAL) and is used to identify photons, electrons and hadrons. Charged and neutral clusters in the electromagnetic calorimeter are separated by extrapolating tracks reconstructed by the tracking system to the calorimeter plane, whilst photons and neutral pions are distinguished by cluster shape and energy distributions. Typically muons are the only particles that penetrate the entirety of the detector and are identified by tracking stations (M1-M5) placed downstream of the calorimeter. Each muon station is a collection of several layers of multiwire proportional chambers interspaced with iron absorbers.

The tracking system provides a measurement of momentum, p, of charged particles with a relative uncertainty that varies from 0.5% at low momentum to 1.0% at 200 GeV/c. The minimum distance of a track to a primary proton-proton collision vertex (PV), the impact parameter (IP), is measured with a resolution of $(15 + 29/p_T)\mu m$, where p_T is the component of p transverse to the beam, in GeV/c [55, 56].

In this analysis simulated events are used to model the effects of detector acceptance and the imposed selection requirements. In the simulation, proton-proton collisions are generated using PYTHIA [57] with a specific LHCb configuration [58]. Decays of unstable particles are described by EVTGEN [59], in which final-state radiation is generated with PHOTOS [60]. The interaction of the generated particles with the detector and its response are implemented using the GEANT4 [61] toolkit as described in Ref. [62]. Charged particles may be deflected into regions where artificial asymmetries manifest. In particular, detection asymmetries may arise due to failures of some of the electronics.

The detector consists of matter thus the interaction cross section with antimatter particles will differ. To minimise potential sources of systematic uncertainties, the polarity of the dipole magnet is regularly reversed.

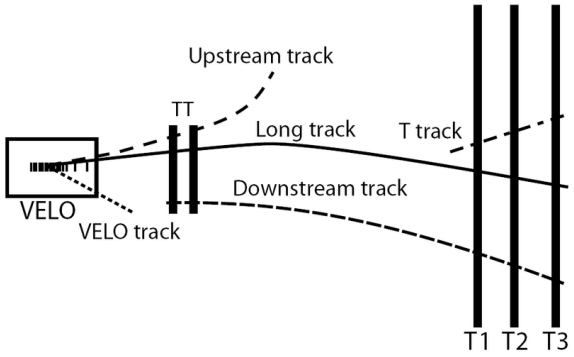


Figure 10: Schematic of possible track types [63].

Due to the design of the LHCb detector, many types of tracks are observed. The possible tracks are shown in Fig. 10. In this analysis, K_S^0 particles are reconstructed in the $K_S^0 \to \pi^+\pi^-$ mode. As K_S^0 is long-lived, many of its decays occur outside of the VELO system. Decays for which the first hits are recorded at the tracking stations (TT), outside of the VELO, are classified as DD since both pion tracks are in the "downstream track" category. Decays that contain hits in the VELO as well as all tracking stations are referred to as LL, since both pion tracks are in the "long track" category.

3.3 The LHCb trigger

The large hadron collider (LHC) operates at a bunch crossing frequency of 40 MHz. Such a volume of information requires immense processing and storage capabilities. Although the production cross sections for b and c-hadrons are substantial, $\rho(pp \to c\bar{c}X) \sim 1.5$ mb, total inelastic scattering cross sections dominate. This results in environments with low signal purities. Therefore the majority of events produced in pp collisions are of little interest. In Run II, the LHCb experiment operated with a limited rate of 12.5 kHz written to storage. To mostly select interesting events requires the use of an efficient trigger system, one capable of reducing the amount of undesirable background saved to tape in real-time.

The LHCb trigger system [64] comprises of three stages applied sequentially. Firstly, the hardware stage referred to as Level 0 (L0), followed by two software stages referred to as Higher Level Triggers (HLT1 and HLT2). A schematic representation of the LHCb trigger is presented in Fig 11. In order to pass to the next level an event must satisfy at least one of the triggers present at the current level. The levels of triggers are as follows:

1. **Level 0 (L0):** a set of custom electronics performs the initial filtering, reducing the input rate from 40 MHz down to 1 MHz. This system relies exclusively on information obtained from calorimeters and the muon stations. Acceptance criteria are based on transverse momenta and transverse energy of particles present in the event.

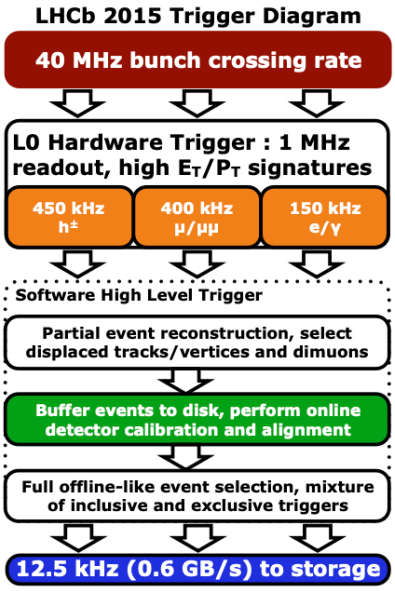


Figure 11: The configuration of the LHCb trigger system during Run II (2016-2018).

2. **Higher Level Trigger 1 (HLT1):** a set of software triggers. At the HLT1 level events are partially reconstructed using tracking information. By leveraging the characteristics of b and c-hadron decays, such as large transverse momenta and significant impact parameter, the input rate of 1 MHz from L0 is reduced down to 110 kHz. Events which pass the HLT1 stage are saved to the Event Filter Farm (EFF) in preparation for the next stage.

3. **Higher Level Trigger 2 (HLT2):** the second software stage and final trigger level. At this stage events are fully reconstructed by considering inputs from all sub-detectors. Specific criteria are imposed on kinematic and geometric properties, reducing the rate from 110 kHz down to 12.5 kHz. Each decay or family of decays of interest posses a corresponding HLT2 line.

Events that pass all levels of the trigger system are saved to storage. When performing an offline analysis is it important to determine whether a trigger was fired by a signal candidate or by an unrelated particle in the event. A category of Trigger On Signal (TOS) is assigned in the instance where a positive trigger decision was satisfied by at least one particle in the decay chain of interest. The category of Trigger Independent of Signal (TIS) refers to an instance in which a particle unrelated to the decay chain in the event satisfies a positive trigger decision.

For Run II, the LHCb experiment enhanced the computing and storage capacity of the EFF. The upgrade to the EFF combined with a strategy to buffer the data between HLT1 and HLT2 extends the allocated time for the HLT2 reconstruction process. In particular, this allows for alignment and calibration to be applied in real-time. Thus, enabling offline-quality information to be obtained within the trigger system. This data collection process, introduced in Run II, is referred to as the Turbo stream. As part of the turbo stream, candidates that pass the HLT2 stage are saved to disk whilst the rest of the event is discarded, significantly reducing storage space for each event (70kb down

to 5kb). This thesis was one of the first analyses to use the output of the Turbo stream at LHCb [65, 66].

4 Data selection and reconstruction

This analysis studies pp collision data at a center-of-mass energy of $\sqrt{s} = 13$ TeV and corresponding integrated luminosity of 5.7 fb^{-1}, collected during Run II (2016-2018) of the LHCb experiment. The aim of this analysis is to obtain a measurement of charm-mixing parameters. By utilising a model-independent approach combined with auxiliary constraints on the strong phases, a feasibility study is performed with the $D^0 \to K^0_S K^+ K^-$ decay mode. The datasets comprise of both LHCb magnet polarities, in the up and down configurations. The stored events have passed specific L0, HLT1 and HLT2 requirements imposed prior to data taking. Additionally, further selections have been optimised and applied offline by this analysis in order to further reduce backgrounds.

4.1 Production modes

There exist two possible production modes for the D^0 mesons. The first involves c-hadrons where prompt D^0 mesons are produced via a strong decay, $D^{*+} \to D^0 \pi^+_s$, in the primary proton-proton interaction. The charge of the associated soft pion, π^+_s, is used to determine the flavour of the D^0 at production. Prompt production occurs at a high rate, however triggering on such decays can be relatively difficult. Two subsamples are studied, "prompt" (Prompt) and "lifetime unbiased prompt" (LTUNB), with different trigger strategies. The differences between the prompt (Prompt) and lifetime unbiased prompt (LTUNB) samples emerge at HLT1 level. The second production mode involves b-hadrons where D^0 mesons are produced via semileptonic (SL) decays, $B^- \to D^0 \mu^- X$ (single-tag) and $\bar{B}^0 \to D^{*+} (\to D^0 \pi^+) \mu^- X$ (double-tag). In this topology X represents a combination of unreconstructed particles such as the anti muon neutrino, $\bar{\nu_\mu}$. The associated muon assists in the triggering, the charge of which defines the flavour of the D^0 meson at production. A schematic of the decay topologies is shown in Fig. 12.

In addition to the data collected by LHCb, this analysis utilities Monte Carlo simulated events. These model the same production mechanisms that exist in the data, in particular prompt decays as well as single-tagged and doubly-tagged semileptonic decays. Two distinct samples of MC events are generated. Firstly the phase-space only sample for which the distribution of the $D^0 \to K^0_S K^+ K^-$ decay mode across the Dalitz plot is governed solely by the acceptance efficiency of the LHCb detector. In the instance of an ideal acceptance this would produce a uniformly populated Dalitz plot. The second employs the use of a simple amplitude model in order to ensure a sufficient number of events in the $a_0(980) \to K^+ K^-$ and $\phi(1020) \to K^+ K^-$ resonance regions which dominate the $D^0 \to K^0_S K^+ K^-$ decay process. In the semileptonic data both the neutral and charged b-hadron decays are reconstructed in a common sample of $B \to D^0 \mu^- X$ events. As such, simulated semileptonic events are generated independently for each production mode and then combined into a single sample. Identical trigger selections are applied

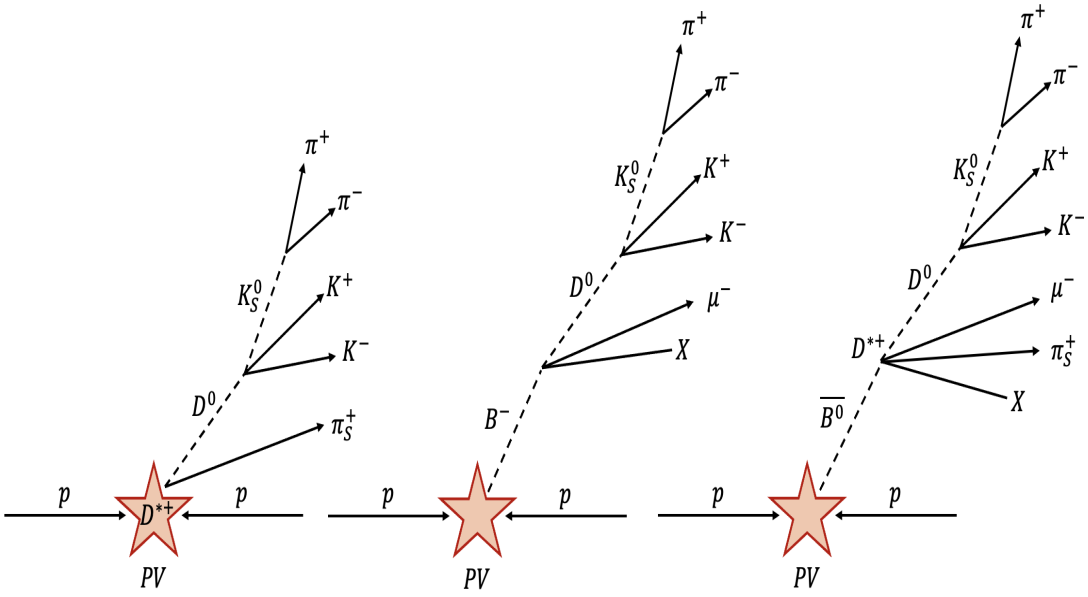


Figure 12: A schematic depicting particle tracks for the prompt (left), semileptonic single-tag decays (right) and semileptonic double-tag decays (right). The primary vertex (PV) refers to the proton-proton collision point.

to the data and simulation. Additionally, the simulated data are truth-matched, meaning that particles throughout the decay chain must have their true associated IDs. The simulated sample incorporates backgrounds such as ghost tracks and radiative decays.

4.2 Selection criteria

The selection criteria used in this analysis exploits behaviour that is characteristic to the decays of b and c-hadrons. Independent selections are applied according to the production mode (trigger strategy) as well as K^0_S decay mode (separately for LL and DD). The variables of particular interest are as follows:

- Kinematic properties that characterise the energy and momenta of particles:
  - The transverse momentum (p_T): the magnitude of the component of the momentum of the particle projected onto the transverse $x-y$ plane:

$$\sqrt{p_x^2 + p_y^2}, \tag{56}$$

    Signal candidates are expected to have significant transverse momentum.

- Geometrical variables related to the spatial position of vertices:
  - Displacement vector (d): defined as the vector connecting the decay vertex (DV) of the parent particle to the primary vertex (PV). The decay vertex is the reconstructed point at which a particle undergoes a decay whilst the primary vertex is the pp collision point. Signal Prompt and LTUNB decays will have almost zero displacement for the D^0 meson whilst for semileptonic production this will be greater than zero.

- Impact Parameter (IP): defined as the distance of closest approach of the reconstructed vertex to the PV. The IP is given by:

$$|d - (d \cdot p)p| \tag{57}$$

where p is the momentum vector. Signal Prompt and LTUNB decays have a small IP for the for the D^0 meson whilst semileptonic production will have a significant IP.

- Transverse Impact Parameter (TIP): defined as the distance of closest approach of the reconstructed vertex to the PV in the transverse $x - y$ plane. The TIP is calculated as follows:

$$\frac{p_x d_y - p_y d_x}{p_T}. \tag{58}$$

For Prompt and LTUNB signal, the TIP will be distributed closely around zero for the D^0 meson whilst in the case of semiletonic production the TIP will have larger values occupying the tails of the distribution.

- Ghost probability: the probability describing the likelihood of the trajectory being that of a real particle. The output is obtained from a multivariate classifier.

- Flight Distance χ^2: the χ^2 distance between the reconstructed DV and PV vectors calculated as:

$$(DV - PV)^T(\text{cov}_{DV} - \text{cov}_{PV})^{-1}(DV - PV), \tag{59}$$

where cov are the associated covariance matricies. The D^0 is expected to have significant Flight Distance χ^2.

- Impact Parameter χ^2 (χ^2_{IP}): the difference in χ^2 of the reconstructed PV fit with and without the particular track under consideration. In contrast to the IP, this quantity also accounts for track uncertainties. For the Prompt and LTUNB samples the signal is expected to have a small Impact Parameter χ^2 for the D^0 meson whilst secondary background candidates will have larger χ^2_{IP} values when the χ^2_{IP} is constructed using the reconstructed D^0 trajectory.

- Particle identification variables:

  - $PIDK$: For a given particle this is the difference in log-likelihood between the kaon hypothesis and the pion hypothesis calculated using information obtained from the RICH detectors.

  - ProbNNk: the probability describing the likelihood of the particle being a kaon. The output is obtained from a neural network. This method uses the same RICH information as the variable above but in a different way and is therefore not fully independent.

4.3 Prompt sample

The prompt sample is selected using the Turbo stream, an approach that encodes offline quality information inside the trigger system, thus eliminating the need for further offline reconstruction. Requirements are imposed on masses and momenta of intermediate particles as well as displacements of final-state charged particles relative to the PV. The candidates pass through the trigger system and further optimisations are applied offline.

4.3.1 L0 requirements

At the hardware level, the D^{*+} meson selection requires that either an unrelated object in the event triggers the selection or that at least one decay product of the D^0 meson satisfies a minimum energy threshold. The final trigger requirement is an inclusive acceptance of events which have been triggered by the particles associated with the charm meson of interest (TOS - Trigger on Signal) and those that have been triggered by other particles in the event (TIS - Trigger Independent of Signal). This is encoded in the following logical condition $Dst_L0Global_TIS \parallel D0_L0Hadron_TOS$ where "$\parallel$" is the logical OR operator.

4.3.2 HLT1 requirements

At the first software stage candidate events can be selected by two possible algorithms: Hlt1TrackMVA and Hlt1TwoTrackMVA. The first searches for a single good quality long track whilst the second searches for pairs of good quality long tracks originating from a common vertex. Both possibilities are applied to D^0 candidates in an inclusive manner, $D0_Hlt1TrackMVA_TOS \parallel D0_Hlt1TwoTrackMVA_TOS$. Due to the decay topology, the HLT1 triggers can introduce significant acceptance effects. These are less severe in the LL sample since all final-state particles, kaons and pions, are produced as long tracks. Therefore any of these particles or pairs of particles could satisfy these triggers. Conversely, for the DD samples it is only the final-state kaons that can satisfy these trigger requirements since the pions are produced downstream of the VELO. The main conditions encoded within the Hlt1TrackMVA line are as follows:

1. The track must have at least 9 hits in the VELO.
2. The quality of track fit satisfies $\chi^2/\text{ndof} < 2.5$.
3. The track is very likely to be real with ghost probabily < 0.4.
4. The track has significant momentum with $p > 3$ GeV/c.

Moreover, a multivariate selection is applied in the $p_t - \chi^2_{IP}$ plane given by the relation:

$$\begin{aligned} &\left[(p_t > 25) \text{ and } (\chi^2_{IP} > 7.4)\right] \\ &\text{or } \left[(1 < p_t < 25) \text{ and } \left(\ln \chi^2_{IP} > \ln(7.4) + \frac{1}{(p_t - 1)^2} + \frac{\alpha(25 - p_t)}{25}\right)\right] \end{aligned} \tag{60}$$

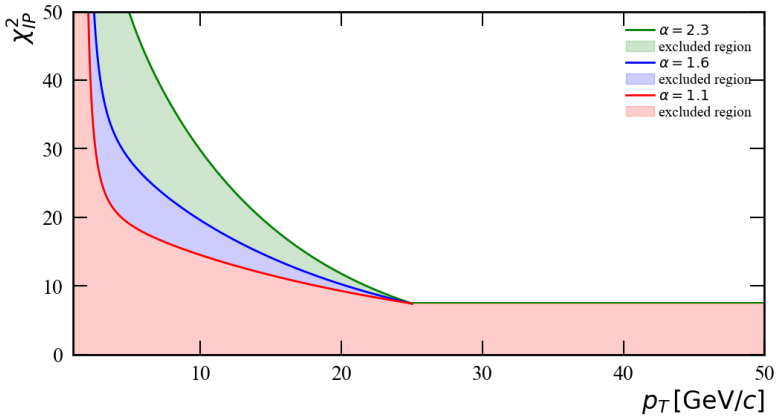


Figure 13: A schematic representation of $p_t - \chi^2_{IP}$ regions excluded by the HltTrackMVA trigger line.

where the quantities are given in units of GeV/c. A visualisation of the accepted candidates is shown in Fig. 13. The parameter α was tightened throughout Run II with values at 1.1, 1.6 and eventually 2.3.

The main difference between the Prompt and LTUNB trigger strategies is that for the LTUNB approach at HLT1 level the D^0 candidate is required to trigger any Hlt1Track line independent of signal (TIS). Examples include the Hlt1TrackMVA and Hlt1TwoTrackMVA lines. This lack of explicit HLT1 requirements preserves the lifetime unbiased nature since criteria imposed at HLT1 level can sculpt the lifetime and phase-space distributions in non-trivial ways.

4.3.3 HLT2 and offline selection

At the final software stage events are fully reconstructed. As such a distinction can now be made between the LL and DD samples. The HLT2 lines used in this analysis are:

- $Hlt2CharmHadDstp2D0Pip_D02KS0KmKp_KS0[LL, DD]Turbo$
- $Hlt2CharmHadDstp2D0Pip_D02KS0KmKp_KS0[LL, DD]_LTUNBTurbo$

with the selection criteria presented in Table 3. In the offline selection the decay chain is additionally reconstructed under kinematic and geometric constraints. A kinematic fit, DecayTreeFitter (DTF), constrains the D^0 and soft pion tracks such that the D^{*+} production vertex coincides with the PV [67], attempting to suppress decays which originate from b-hadrons (secondary decays). Moreover, D^0 and K^0_S masses are fixed to their known values in the kinematic fit to improve the resolution of the "Dalitz plot" coordinates (Dalitz variables).

In order to reduce background contamination, requirements are imposed on the quality of kinematic fits and properties such as vertex and track displacements, particle-identification and invariant masses. In particular, contributions of $D^0 \to \pi^+\pi^-K^+K^-$ decays are reduced by selecting a region in the $\pi^+\pi^-$ invariant mass, reconstructed with a primary vertex constraint, around the known K^0_S mass. Also, the K^0_S decay vertex must be significantly displaced with respect to the D^0 decay vertex. For the D^0 meson, signal

LL and DD candidates must reside within a mass window $m(K^0_s K^+ K^-) \in [1840, 1890]$ MeV/c^2. The reconstructed mass of the soft pion, with a PV constraint and K^0_S mass constraint, is given by $\Delta m = m(K^0_s K^+ K^- \pi^+_s) - m(K^0_s K^+ K^-)$ and selected candidates must be within the region $\Delta m \in [139.57, 156]$ MeV/c^2 for both LL and DD samples. Particle-identification constraints are applied on the probability that the final state tracks are kaons. Simulated samples are selected identically and taken as signal whilst the background corresponds to real data residing in the D^0 mass side-band, region outside of the mass acceptance. Example distributions are shown in Fig 14.

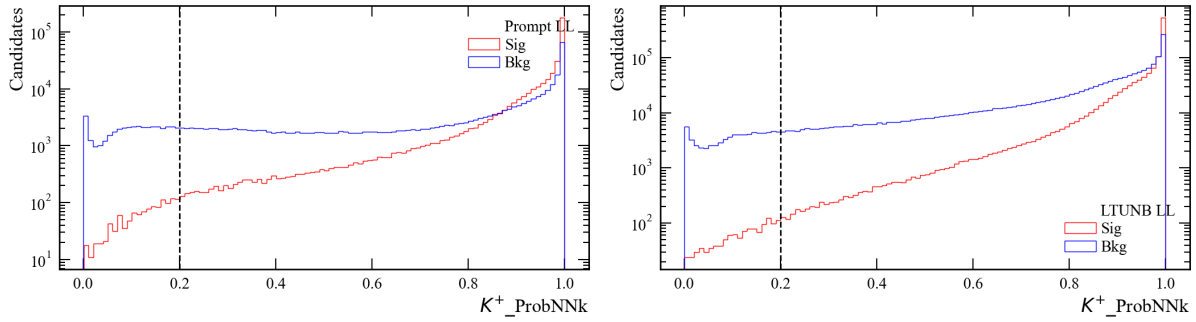


Figure 14: Distributions showing the probability of a kaon hypothesis. The Prompt and LTUNB LL samples have been used for illustration purposes. Events to the right of the dashed vertical line are selected.

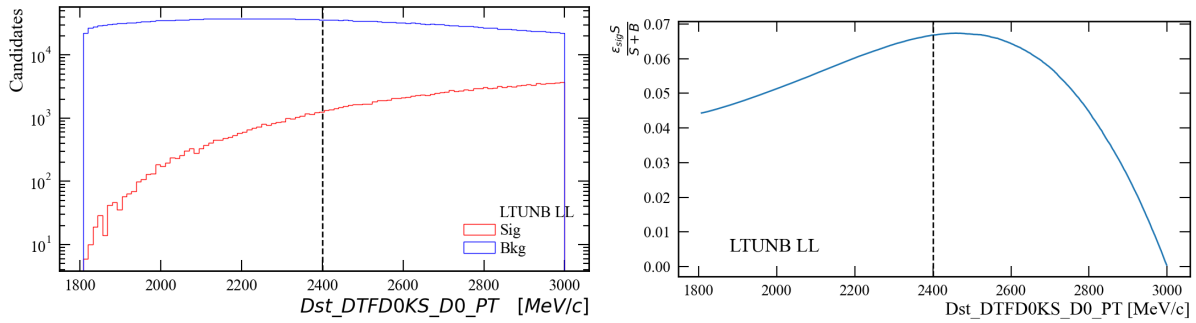


Figure 15: Scan of the D^0 transverse momentum for the LTUNB LL sample. The product of signal selection efficiency (ϵ_{sig}) and signal purity ($\frac{S}{S+B}$) is used as a figure of merit to impose the selection criteria. Events to the right of the dashed vertical line are selected.

The selection procedure for the LTUNB sample results in a much lower purity when compared to that of the lifetime biased prompt sample. To increase the signal purity, further optimisations are performed. The most discriminating variables are ones associated with kinematic and geometric properties of the D^0 mesons. For example, the biased prompt HLT2 selection requires a significant displacement from the primary vertex, however this biases the distribution of the decay-time acceptance efficiency. To mitigate this, the reconstructed transverse momentum of the D^0 is considered instead. By utilising the product of the signal acceptance efficiency with signal purity, a scan is performed as a function of transverse momentum, the results of which are presented in Fig 15. The transverse momentum has been obtained from the same constrained fit as that of the Dalitz variables. To suppress backgrounds such as $D^{*0} \to D^0 \pi^0$ with $\pi^0 \to e^+ e^- \gamma$, a

Table 3: HLT2 trigger requirements.

Particle	Variable	Requirement
$\pi^{\pm}$ of K^0_S	Track χ^2/ndof	< 3 (LL)
	Track χ^2/ndof	< 4 (DD)
	IP χ^2	> 3 (LL)
	Momentum	> 3 GeV/c (DD)
	Transverse momentum	> 175 MeV/c (DD)
K^0_S	$\lvert m(\pi^+\pi^-) - 497.648\rvert$	< 35 MeV/c^2 (LL)
		< 64 MeV/c^2 (DD)
	Vertex-fit χ^2/ndof	< 30
	Decay-time with respect to PV	> 2 ps (Prompt LL)
		> 0.5 ps (Prompt DD)
	z postion of the vertex	$\in [-0.1, 0.5]$ m (LL)
		$\in [0.4, 2.275]$ m (DD)
	Logarithm of the decay-length χ^2	> 5 (2017-2018)
$K^{\pm}$ of D^0	Track χ^2/ndof	< 3
	Track-based ghost probability	< 0.4
	Momentum	> 1000 MeV/c
	Transverse momentum	> 500 MeV/c (LTUNB)
	Impact parameter χ^2	> 4 (Prompt)
	PIDK	> 5
D^0	Mass	$\in [1.765, 1.965]$ GeV/c^2
	Vertex-fit χ^2/ndof	< 20 (2016)
		< 5 (2017-2018)
	$\sum p_T$	> 1.5 GeV/c
	Transverse momentum	> 1.8 GeV/c
	Direction angle	< 34.6 mrad
	Flight distance χ^2	> 20 (Prompt)
	Decay time	> 0.1 ps (Prompt)
		> 0.25 ps (LTUNB)
$\pi^{\pm}_s$	Track χ^2/ndof	< 3
	Track-based ghost probability	< 0.4 (2016)
		< 0.25 (2017-2018)
	Momentum	> 1 GeV/c
	Transverse momentum	> 100 MeV/c (2016)
		> 200 MeV/c (2017-2018)
$D^{*\pm}$	Vertex-fit χ^2/ndof	< 10
	$m(D^*) - m(D^0)$	$\in [135, 165]$ MeV/c^2
TisTos	$Dst_Hlt1 * MVA * _TOS$ (Prompt 2016)	
	$Dst_Hlt1 * Track * _TOS$ (Prompt $2017 - 2018$)	
	$Dst_Hlt1 * MVA * _TIS$ (LTUNB 2016)	
	$Dst_Hlt1 * Track * _TIS$ (LTUNB $2017 - 2018$)	

requirement on PIDe is included. The PIDe variable is inspected to ensure the slow pion is incompatible with electron hypothesis. Lastly all tracks are required to have a distinct set of hits in the VELO, in order to remove any duplicated tracks (cloned tracks). An outline of the offline selection is given in Table 4.

Table 4: Prompt offline selection.

Particle	Variable	Requirement
K_S^0	Mass	$\in [485, 510]$ MeV/c^2 (LL)
		$\in [478, 520]$ MeV/c^2 (DD)
	Logarithm of the decay-length χ^2	> 5
	Decay time	> 0
	Transverse momentum	> 200 MeV/c
$K^\pm$	PIDK	> 0.2
D^0	Mass	$\in [1.84, 1.89]$ GeV/c^2
	Vertex-fit χ^2/ndof	< 5
	$\lvert TIP \rvert$	< 80 μm
	IPχ^2	< 9
	Decay time	$\in [0.3, 8]\tau$
	DTF Transverse momentum	> 2400 MeV/c (LTUNB)
$\pi_s^\pm$	Track-based ghost probability	< 0.25
	Transverse momentum	> 200 MeV/c
	IP χ^2	< 25
	PIDe	< 4
$D^{*\pm}$	DTF χ^2/ndof	$\in [0, 6]$
	Δm	$\in [139.57, 156]$ MeV/c^2
L0	$D0_L0Hadron_TOS \parallel Dst_L0Global_TIS$	
HLT1	$D0_Hlt1TrackMVA_TOS \parallel D0_Hlt1TwoTrackMVA_TOS$ (Prompt)	
All tracks	Required not to use identical set of VELO hits	

4.4 Semileptonic sample (SL)

The reconstruction procedure for the SL sample follows a process referred to as "stripping" and is used for the majority of decay modes studied at LHCb. In particular, events sequentially pass through the hardware and trigger stages, with raw sub-detector data eventually saved to tape. The raw data comprise of many possible decay modes, as such a full event reconstruction is applied offline to search for the decay mode of interest. In contrast, the Turbo lines perform a full event reconstruction and search for specific decays in real time whilst the detector is in operation. The offline selection of the $b2D0MuXKsLL[LL, DD]CharmFromBSemiLine$ stripping lines is presented in Table 5.

The stripping selection has been designed specifically for the $B \to D^0\mu X$ decay topology. In the reconstruction process, a distinction is not made between charged and neu-

Table 5: Semileptonic stripping selection.

Particle	Variable	Requirement
$\pi^{\pm}$ of K^0_S	Track χ^2/ndof	< 4
	Momentum	> 2 GeV/c
	IPχ^2 with respect to PV	> 9 (LL)
		> 4 (DD)
	Track-based ghost probability	< 0.5
K^0_S	$\lvert m(\pi^+\pi^-) - 497.648\rvert$	< 35 MeV/c^2 (LL)
		< 64 MeV/c^2 (DD)
	Track χ^2/ndof	< 6
	Cosine of direction angle	> 0.99
	Distance of closest approach χ^2	< 30 (LL)
		< 25 (DD)
	Vertex fit χ^2/ndof	< 25
	Flight distance χ^2	> 4 (LL)
	Momentum	> 2 GeV/c (LL)
		> 3 GeV/c (DD)
	Transverse momentum	> 250 MeV/c
$K^{\pm}$ of D^0	Track χ^2/ndof	< 4
	Track-based ghost probability	< 0.5
	Momentum	> 2 GeV/c
	Transverse momentum	> 250 MeV/c
	IPχ^2 with respect to PV	> 4
	PIDK	> -5
D^0	Mass	$\in [1.765, 1.965]$ GeV/c^2
	$\sum p_T$	> 1.4 GeV/c
	Transverse momentum	> 2 GeV/c
	Distance of closest approach χ^2	< 20
	Vertex fit χ^2/ndof	< 6
	z vertex distance to PV	> -10.0 mm
$\mu^{\pm}$	Track χ^2/ndof	< 4
	Transverse momentum	> 800 MeV/c
	Momentum	> 3 GeV/c
	Track-based ghost probability	< 0.5
	IPχ^2 with respect to PV	> 4
	PIDμ	> 0
B	Vertex fit χ^2/ndof	< 6
	Mass	$\in [2500, 6000]$ MeV/c^2
	$m(D^0\mu^-)$	< 6200 MeV/c^2
	Cosine of direction angle	> 0.999
	z vertex distance to PV	> -9999 mm
TisTos	$Hlt1_*Track*_TOS \parallel Hlt2Topo*_TOS \parallel$ $Hlt2_*SingleMuon*_TOS \parallel Hlt2Global_TIS$	

tral B meson production modes. At the hardware trigger stage each observed event is required to contain at least one displaced muon track with a high transverse momentum whilst at the software stage B candidates are selected by a topological trigger which considers two, three and four-body final states [68]. Additionally a displaced vertex consistent with the decay of a b-hadron is required. Initially, particle tracks are fit without external constraints and the masses of the D^0 and K^0_S particles are fixed to their known values in the reconstruction of Dalitz coordinates. The visible B mass is formed using candidate $D^0\mu^-$ pairs and is required to be within the region $m(D^0\mu^-) \in [2500, 5200]$ MeV/c^2 whilst the mass of the D^0 candidate, reconstruction with a K^0_S mass constraint, must satisfy $m(K^0_s K^+K^-) \in [1800, 1930]$ MeV/c^2. Due to the presence of unreconstructed particles in the final state, a variable termed the "corrected mass" is introduced to eliminate background contributions. The corrected mass is defined as $\sqrt{m^2(D^0\mu^-) + p_T^2(D^0\mu^-)} + p_T(D^0\mu^-)$, where $p_T(D^0\mu^-)$ is the component of momentum transverse to the flight direction of the B meson and partially compensates for absent decay products. The corrected mass is required to be less than 6500 MeV/c^2 for both the LL and DD samples. Other background contributions are reduced by imposing flight-distance and mass criteria on the K^0_S candidates as shown in Fig. 17. Particle identification constraints are applied on the probability that the final-state tracks are kaons. Simulated samples are selected identically and taken as signal whilst the background corresponds to real data residing in the D^0 mass side-band, which is the region outside of the mass acceptance. Example distributions are shown in Fig 16. Lastly all tracks are required to have a distinct set of hits in the VELO, this removes any clones. The full offline selection is presented in Table 6.

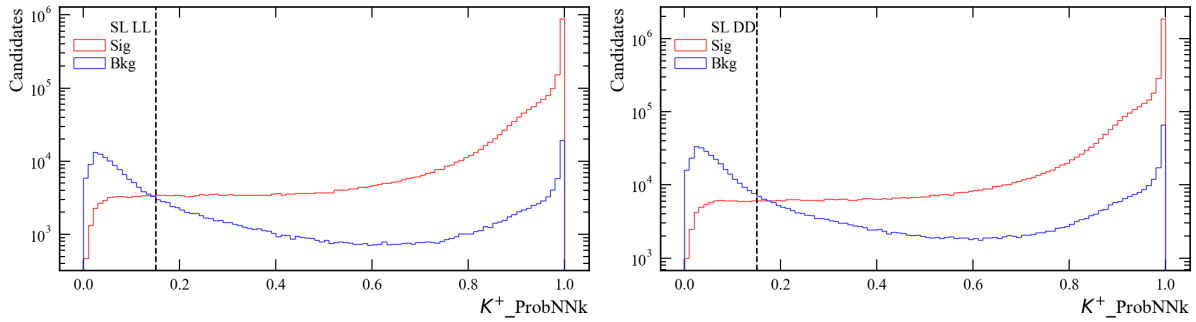


Figure 16: Distributions showing the probability of a kaon hypothesis. Only the positive kaons have been shown for illustration purposes. Events to the right of the dashed vertical line are selected.

Following the prompt and SL selection procedures, there may exist some overlap between the samples. In order to ensure statistically independent datasets, overlapping candidates are removed. In particular, a hierarchy of LTUNB, SL and prompt is established, with the LTUNB sample at the top. As such, any overlapping candidates are always removed from a sample lower in the hierarchy. Additionally, there may exist multiple candidates reconstructed from the same event. All candidates are checked; if at least two candidates have an identical run number and event number, then only one is

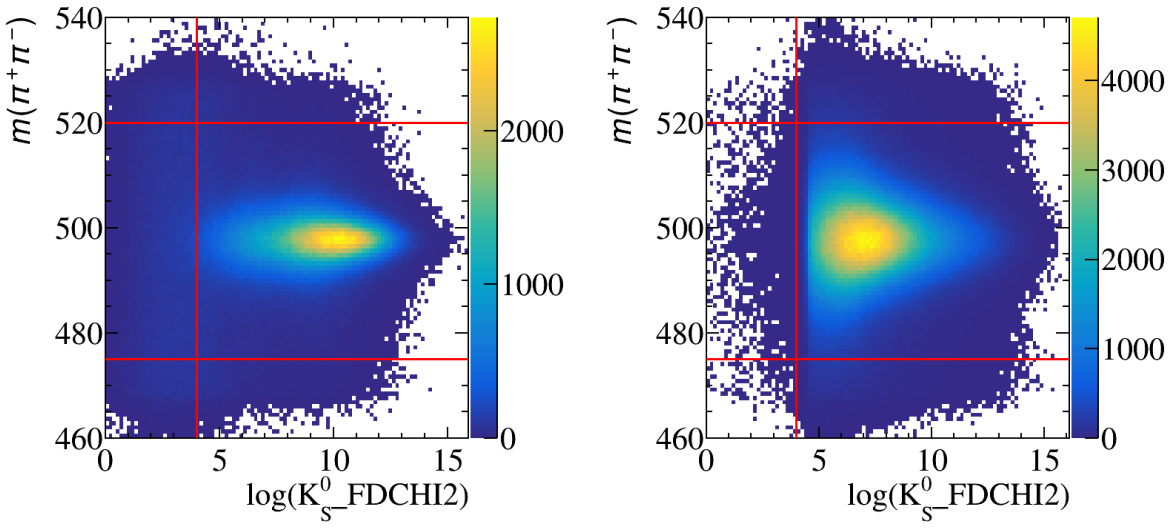


Figure 17: A visualisation of the K^0_S flight distance χ^2 with respect to the D^0 decay vertex vs $m(\pi^+\pi^-)$ for the LL (left) and DD (right) samples. Events to the right of the red vertical line and in-between the red horizontal lines are selected.

Table 6: SL offline selection.

Particle	Variable	Requirement
K^0_S	Mass	$\in [475, 520]$ MeV/c^2
	Logarithm of the decay-length χ^2	> 4
$K^\pm$	ProbNNk	> 0.15
D^0	Mass	$\in [1.8, 1.93]$ GeV/c^2
	Vertex-fit χ^2/ndof	< 6
	Decay time	$\in [0, 20]\tau$
L0	μ_L0Muon_TOS	
HLT1	$\mu_Hlt1TrackMuon_TOS \parallel \mu_Hlt1TrackMuonMVA_TOS$	
HLT2	$B_TopoMu[2,3,4]Body_TOS$	
All tracks	Required not to use identical set of VELO hits	

retained at random [69]. The overlap and multiple candidate fractions are presented in Table 7.

Sample	Overlapping Candidates [%]		Multiple Candidates [%]	
	LL	DD	LL	DD
Prompt	14.97	17.15	6.22	4.31
LTUNB	-	-	9.66	8.18
SL	0.53	0.63	1.41	1.36

Table 7: Fractions of removed overlapping and multiple candidates. Overlapping candidates are removed first followed by any remaining multiple candidates.

4.5 Determination of signal yields

Samples are treated independently according to K^0_S category. Signal yields in each of the subsamples are determined either by fitting the Δm distribution for the Prompt and LTUNB samples, or the $m(K^0_S K^+ K^-)$ distribution for the semileptonic sample. The mass-difference distribution is modelled as a combination of D^{*+} signal and a smooth background dominated by real D^0 decays incorrectly combined with a random pion not associated with the D^0 or D^{*+} decay. For the semileptonic sample the D^0 distribution is modelled as a combination of true D^0 signal and a smooth background consisting of random D^0 meson combinations. In both production modes the signal distribution is empirically described by a combination of a core Johnson S_U distribution and a a floating Gaussian with a shifted mean $\Delta\mu$. The Johnson S_U [70] is defined as:

$$\mathcal{F}(x|\sigma,\mu,\delta,\gamma) = \frac{1}{N}\frac{e^{-\frac{1}{2}\left[\gamma+\delta\sinh^{-1}\left(\frac{x-\mu}{\sigma}\right)\right]^2}}{\sqrt{1+\left(\frac{x-\mu}{\sigma}\right)^2}}, \tag{61}$$

where δ and γ are tail parameters, while μ is the mode of the distribution, σ governs the dispersion of the the core and N is the normalisation. The full signal probability density can be written as:

$$\mathfrak{F}(x) = f\mathcal{F}(x|\sigma,\mu,\delta,\gamma) + (1-f)F(x|\Delta\mu, s\sigma), \tag{62}$$

where f describes the proportions of components and s is a factor which scales the width. The semileptonic background probability density is described using a second-order Chebyshev polynomial whilst an empirical function based on a two-body phase-space model is used for the prompt samples:

$$\mathfrak{F}(\Delta m) = (m_0 - \Delta m)^\alpha e^{-\beta(m_0-\Delta m)}, \tag{63}$$

where α and β are floating parameters and m_0 is the known mass of the charged pion.

Signal yields are extracted using a binned extended maximum-likelihood fit such that the mass window is partitioned into 180 and 100 bins for the prompt and semileptoinic samples, respectively.

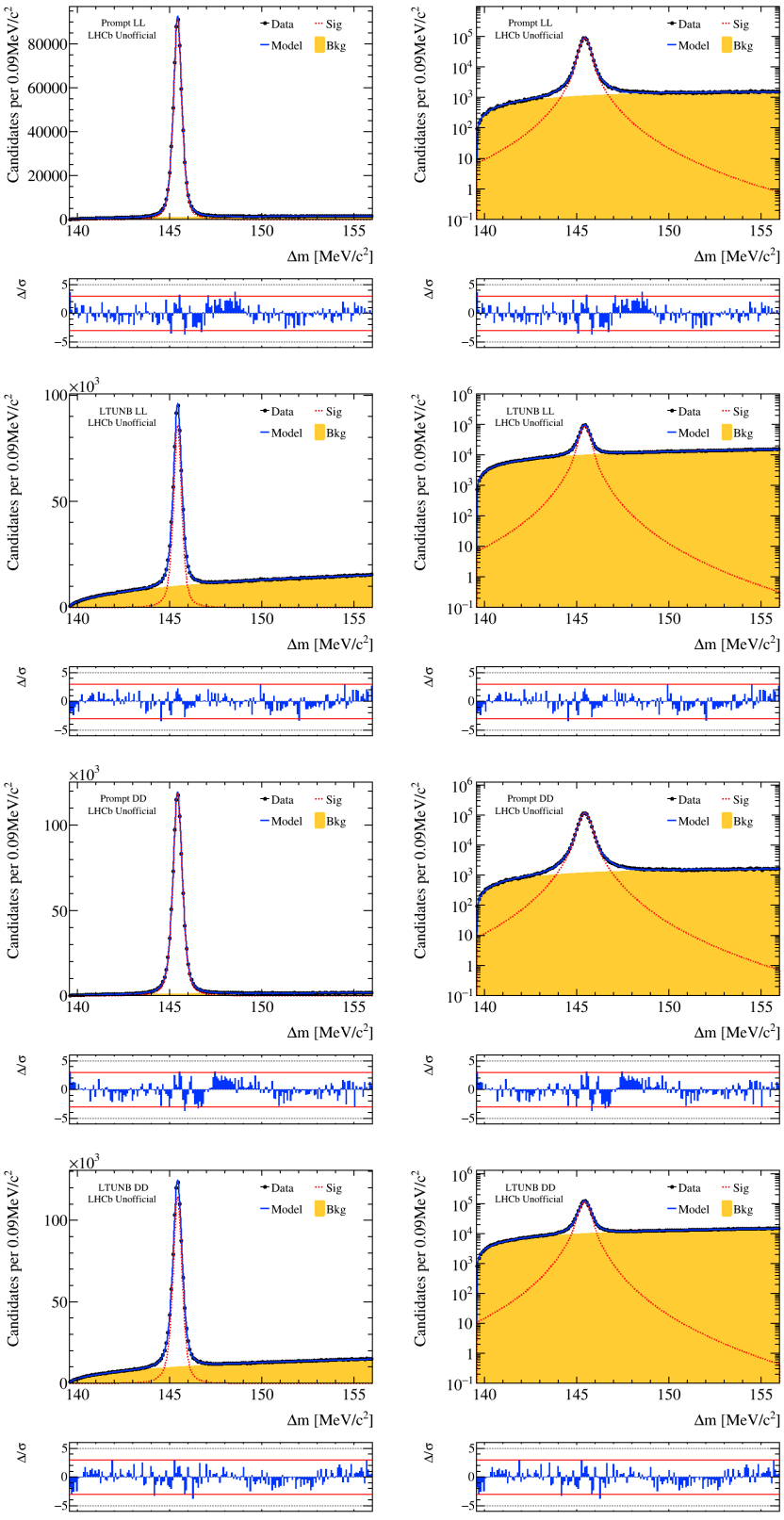


Figure 18: Fits to the Prompt and LTUNB Δm distributions showing linear (left) and log scale (right) projections. The top four plots present the LL samples whilst the bottom four plots present the DD samples. The fit function is described in the main text.

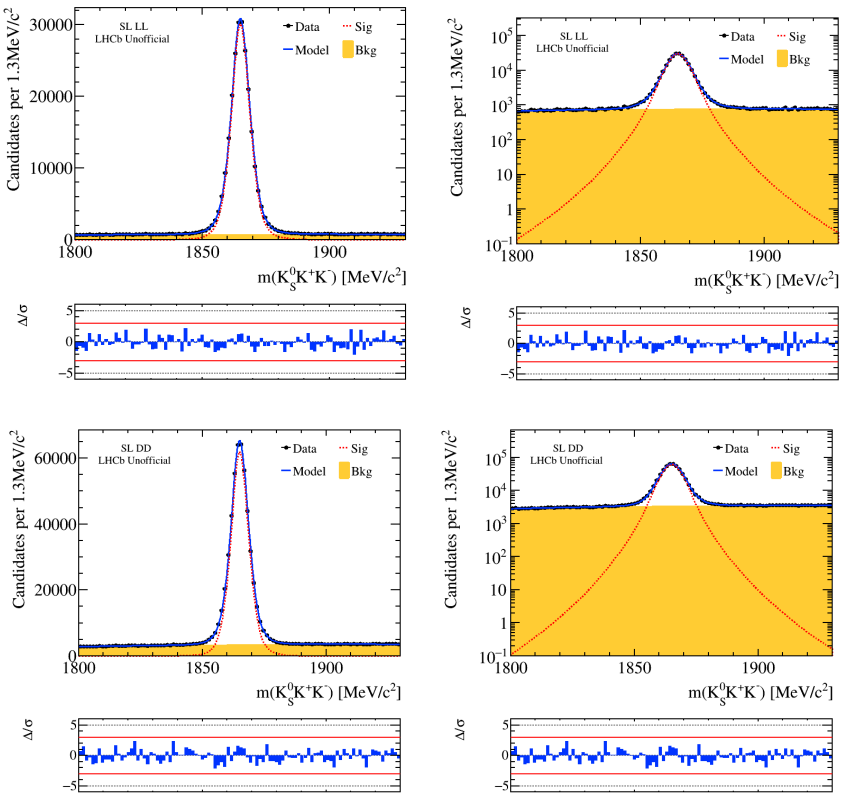


Figure 19: Fits to the semileptonic $m(K^0_S K^+ K^-)$ distributions showing linear (left) and log scale (right) projections. The top row presents the LL sample whilst the bottom row presents the DD sample. The fit function is described in the main text.

The fitted yields are presented in Table. 8. The obtained sample yields sum to a total of approximately three million and seven hundred thousand candidates. The global purity is calculated by considering the entirety of the corresponding mass windows whilst the signal region is defined such that $\Delta m \in [143, 147]$ MeV/c^2 and $m(K^0_S K^+ K^-) \in [1845, 1885]$ MeV/c^2. It is evident that for the Prompt production mode the DD sample has the higher purity whilst for the SL production mode the LL sample has the higher purity. This suggests that the procedure selection procedure can be further optimised. Potentially a multivariate classifier could be trained in order to improve the offline selection strategy for the SL DD sample.

Table 8: Fitted signal yields and corresponding purities obtained for the prompt, prompt unbiased and semileptonic samples.

Sample	Signal Yield		Purity (Global)		Purity (Signal Region)	
	LL	DD	LL	DD	LL	DD
Prompt	$652,655 \pm 978$	$938,726 \pm 1201$	0.752	0.804	0.929	0.947
LTUNB	$611,222 \pm 935$	$903,273 \pm 1158$	0.237	0.316	0.585	0.674
SL	$226,770 \pm 598$	$396,543 \pm 776$	0.749	0.554	0.904	0.809

The Δm distributions for the Prompt and LTUNB samples are provided in Fig. 18 and the

$m(K^0_S K^+ K^-)$ distribution for the semileptonic sample are shown in Fig. 19. To illustrate the resonant structure of the $D^0 \to K^0_S K^+ K^-$ decay, example Dalitz plots are provided in Fig. 20. The $\phi(1020) \to K^+ K^-$ two-body resonant state appears as a dark band on the Dalitz plot. In addition, the $a_0(980)$ state also appears beneath the ϕ resonance.

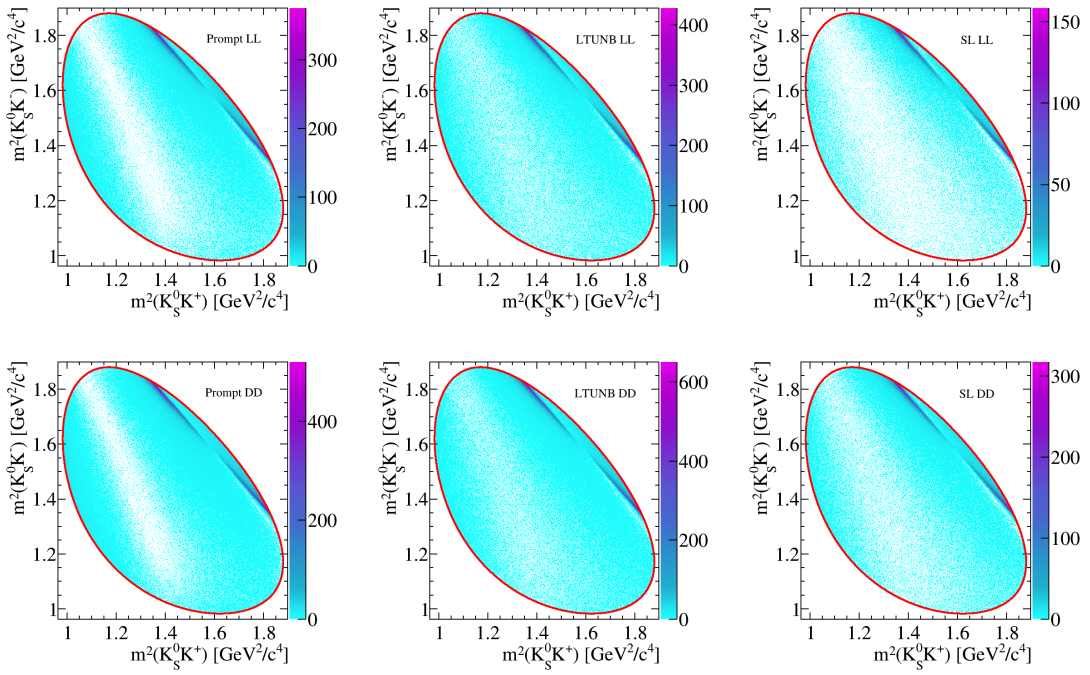


Figure 20: Background subtracted and not acceptance corrected Dalitz plots. The $\phi \to K^+ K^-$ resonance appears as the dark band in the upper right part of the Dalitz plane.

4.6 Comparison with $D^0 \to K^0_S \pi^+ \pi^-$ decays

The observed yields can be compared with that of a sister channel, $D^0 \to K^0_S \pi^+ \pi^-$, which is isolated with a selection that closely follows the selection strategy outlined previously for the decay mode $D^0 \to K^0_S h^+ h^-$. The ratio of branching fractions for $K^0_S K^+ K^-$ to $K^0_S \pi^+ \pi^-$ decays is 0.158 ± 0.015 [71]. The fitted yields, split by K^0_S category, are shown in Table 9. A clear discrepancy with respect to expectation is observed for the prompt sample as the ratios of yields are smaller by factors of 2.72 and 2.94 for the LL and DD respective categories. This effect has been studied and is believed to be caused by the criteria imposed on the $p_t - \chi^2_{IP}$ plane encoded within the Hlt1TrackMVA and Hlt1TwoTrackMVA trigger lines. Since these lines require good quality long tracks, in the case of the DD samples such criteria can only be satisfied by the final state kaons. Additionally the IPχ^2 selection with respect to PV in the semileptonic stripping line introduces a smaller yet similar bias. The phase space structure of the $K^0_S K^+ K^-$ final state is dominated by the $\phi(1020)$ resonance which decays into two kaons. By studying simulated samples, the final state kaons were found to be mainly distributed at lower IPχ^2 values. Stringent selection criteria imposed on the quality of the kaon tracks disproportionately removes signal candidates. The observed yields for the LTUNB production are consistent

with expectation whilst the semileptonic production mode also shows a discrepancy with respect to the $D^0 \to K^0_S\pi^+\pi^-$ expectation, however the effect is smaller.

Table 9: Fitted yields obtained for the $D^0 \to K^0_S\pi^+\pi^-$ decay mode. The ratio R_{obs} is defined as $R_{obs} = \frac{N_{KK}}{N_{\pi\pi}}$.

Sample	$D^0 \to K^0_S\pi^+\pi^-$		$\frac{R_{obs}}{R_{PDG}}$	
	LL	DD	LL	DD
Prompt	$11,239,630 \pm 4,173$	$17,462,771 \pm 4,807$	0.368 ± 0.035	0.340 ± 0.032
LTUNB	$3,049,259 \pm 4,966$	$4,957,550 \pm 5,474$	1.269 ± 0.120	1.153 ± 0.109
SL	$1,973,751 \pm 1,802$	$3,274,266 \pm 6,091$	0.727 ± 0.069	0.767 ± 0.073

The reconstruction and selection procedures can introduce unwanted biases in the data. In particular, stringent selection requirements will impact the selection efficiency as a function of D^0 lifetime and position in the Dalitz plane. Additionally, a finite detector resolution can result in the migration of data points between decay-time and Dalitz bins. This sculpts the acceptance within a bin and across bins, leading to a degradation in sensitivity. The bin-flip method is designed to suppress such acceptance effects by taking the ratios of yields observed in kinematically similar bin pairs, reconstructed on opposite sides of the principal bisector of the Dalitz plot. To further minimise the possible impact of efficiency effects, corrections are applied to the data. The experimental effects are modeled for each of the prompt, lifetime unbiased prompt and semileptonic samples. Furthermore, the two categories of K^0_S decay are studied separately. Understanding acceptance effects is critical in order to apply necessary corrections to the data prior to the final fit and also when evaluating systematic uncertainties.

4.7 Detector resolution

The experimental resolution, defined as the width of the distribution of the difference between the reconstructed and its true value, is obtained using simulated samples. The resolution arises due to the finite spatial and temporal precision of the detector components. The simulation considers both phase-space and resonant decays, selected and reconstructed in a manner identical to that of the data. For example, the decay-time resolution is given by the standard deviation of each of the distributions presented in Fig. 21. The decay-time resolution can be ignored in this analysis method since the mixing period is much lesser than the decay-time, however the decay-time acceptance is studied and can be used to assign systematic uncertainties. The decay-time resolution is estimated using simulation to vary between 0.24 and 0.35 lifetimes.

The resolution for the Dalitz coordinates is determined using a two-dimensional consideration of the $m^2(K^0_S K^+)$ and $m^2(K^0_S K^-)$ invariant masses. Due to the kinematic constraint on the K^0_S mass, imposed as part of the reconstruction process, an anti-correlation between resolutions of the two Dalitz variables is observed and presented in Fig. 22. Al-

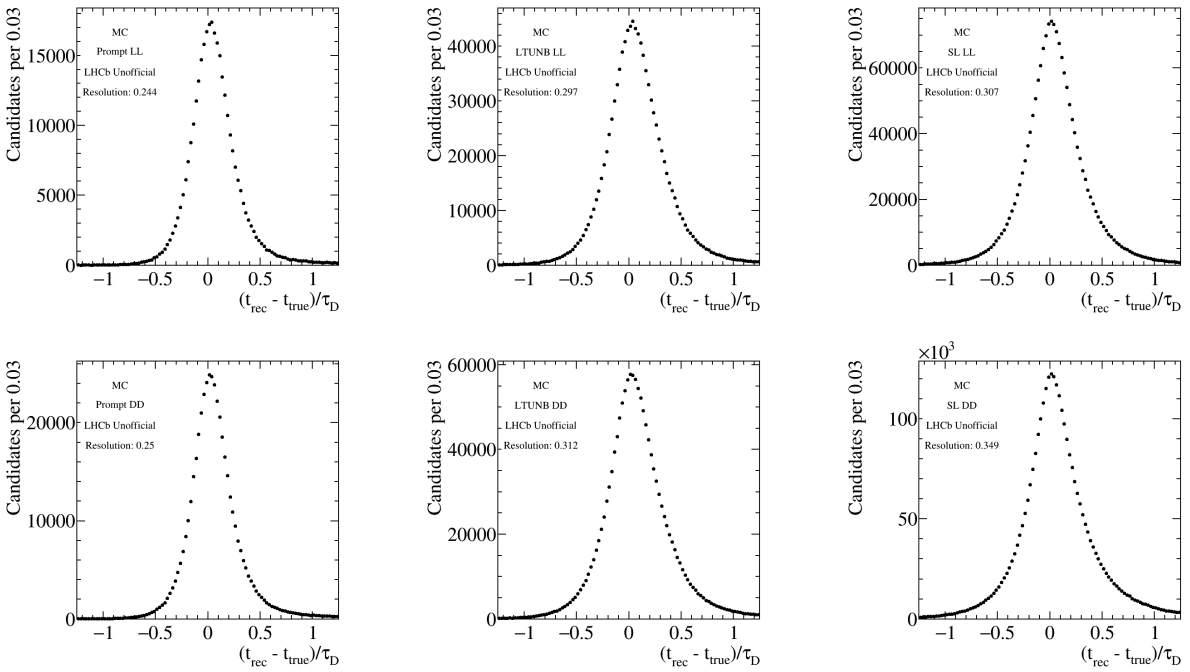


Figure 21: Distributions showing the differences between the reconstructed and generated D^0 lifetime for the prompt (left), lifetime unbiased prompt (middle) and semileptonic (right) samples. The K^0_S LL category is presented on the top row whilst the D^0_S DD category is presented on the bottom row.

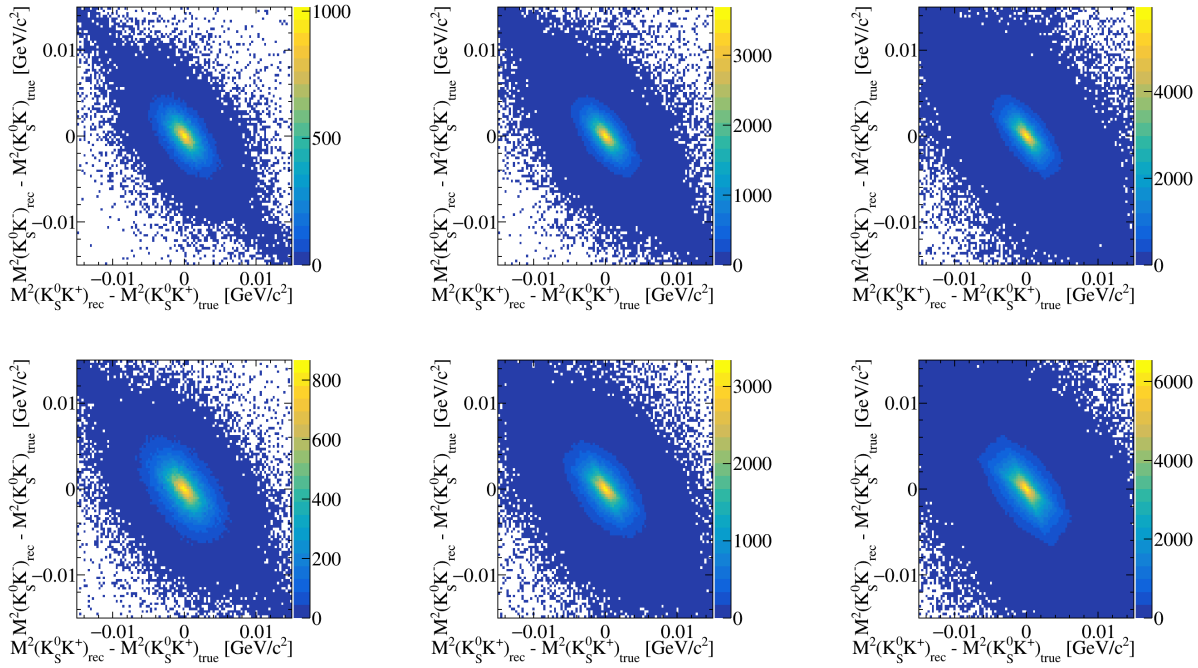


Figure 22: Distributions showing the differences between the reconstructed and generated Dalitz coordinates for the prompt (left), lifetime unbiased prompt (middle) and semileptonic (right) samples. The K^0_S LL category is presented on the top row whilst the K^0_S DD category is presented on the bottom row.

though the resolution on the Dalitz coordinates appears to be much narrower than the size of the considered Dalitz bins, candidates residing near a boundary edge can migrate between bins. As such, the Dalitz resolution is ignored in the final bin-flip fit.

4.8 Efficiency variation as a function of decay-time

In an ideal scenario the D^0 decay-time is expected to follow an exponential decay. Due to the precision of the detector, each of the measured decay-time values is Gaussian distributed. The decay-time distribution is modeled as a product of two contributions. The first contribution is a convolution of an exponential of a known lifetime with a detector resolution model obtained from simulation. The second contribution is an efficiency function given by :

$$\epsilon(t) = \frac{(t - t_0)^n}{a + b(t - t_0)^n} e^{\beta t}, \tag{64}$$

where t is the decay-time, t_0 is the lowest accepted decay-time, whilst a,b,n and β are free parameters. The fits to the D^0 lifetimes obtained using simulated samples are presented in Fig. 23 and the corresponding decay-time acceptance efficiencies are shown in Fig. 24.

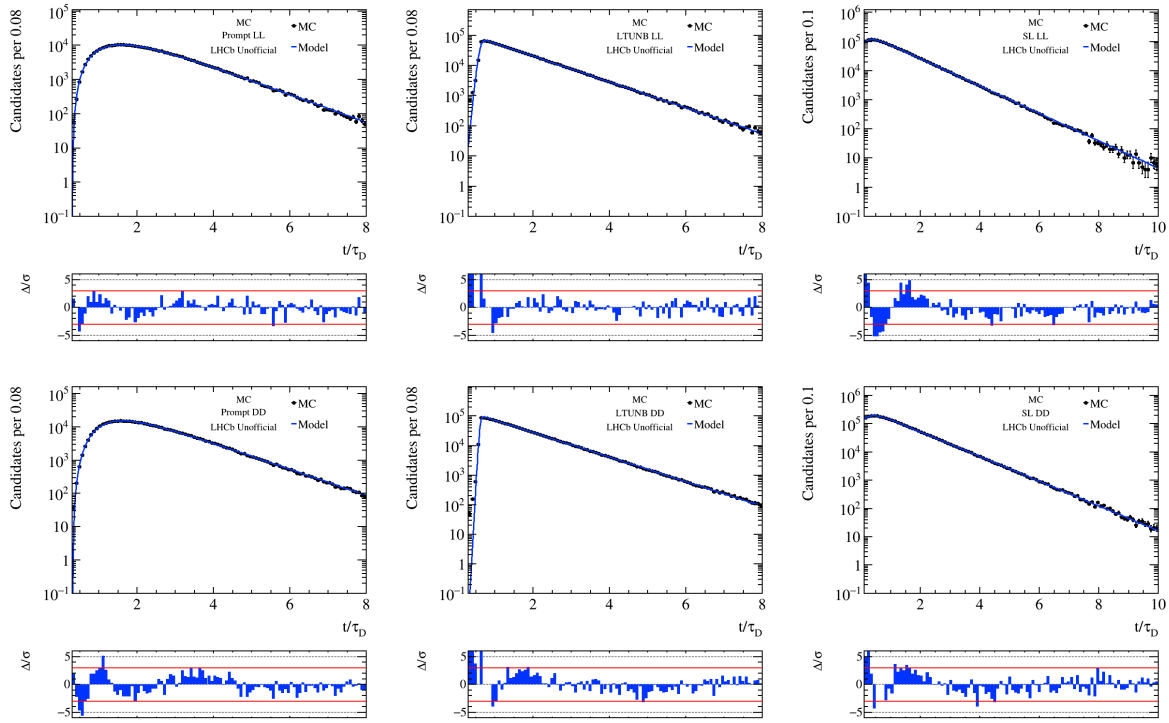


Figure 23: Plots showing fits to the reconstructed D^0 decay-time obtained using simulated samples for the prompt (left), lifetime unbiased prompt (middle) and semileptonic (right) samples. The K^0_S LL category is presented on the top row whilst the D^0_S DD category is presented on the bottom row. The top part of each plot shows the simulated data and model whilst the bottom part shows the pulls.

Evidently, the relative efficiency is lower for the prompt sample, especially at low decay-time. The degraded efficiency is primarily caused by displacement requirements on

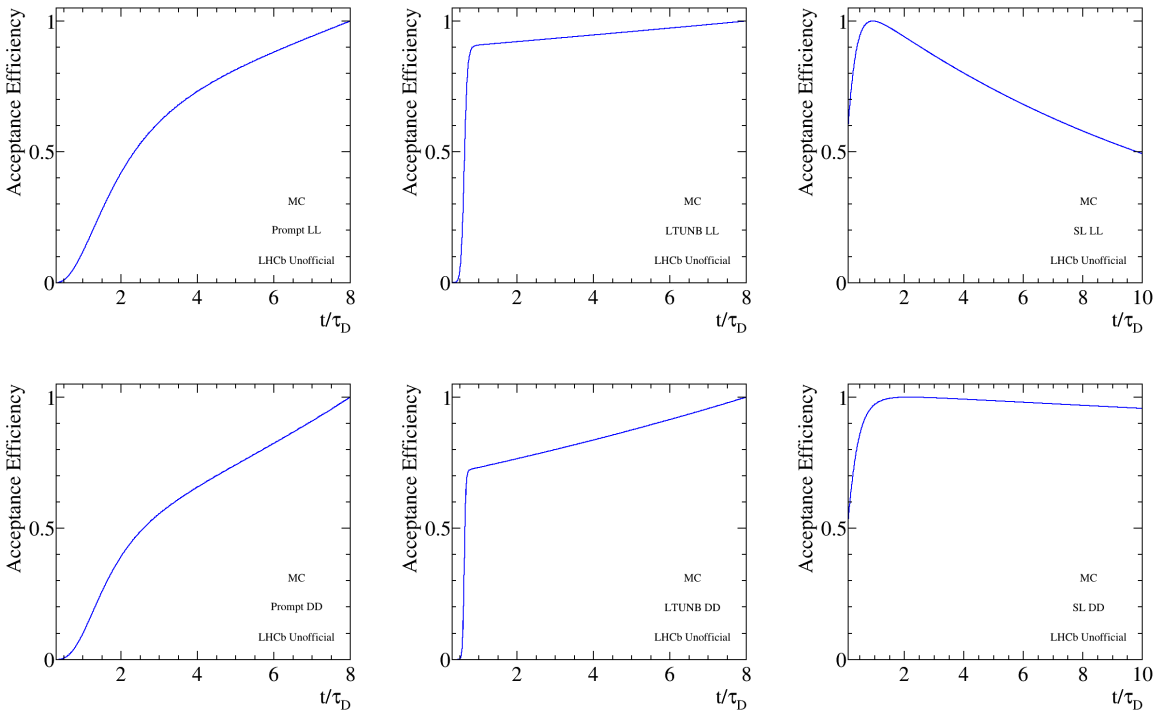


Figure 24: Plots showing the reconstructed D^0 lifetime acceptance distributions obtained using simulated samples for the prompt (left), lifetime unbiased prompt (middle) and semileptonic (right) samples. The K^0_S LL category is presented on the top row whilst the K^0_S DD category is presented on the bottom row.

the D^0 final state particles in the trigger. Since the decay-time acceptance is expected to be symmetric with respect to the principal bisector, the effect of the decay-time acceptance should almost completely cancel in the binflip approach of forming a ratio between signal yields on opposite sides of the Dalitz plot.

4.9 Efficiency variation across the Dalitz plot

In a similar manner to that of the decay-time acceptance, efficiency variation over the Dalitz plane is expected to cancel when forming ratios of signal yields in regions which are kinematically identical. It is critical that the efficiency variation does not significantly alter the average strong-interaction phases for which auxiliary measurements are used. This effect is minimised by adopting a binning scheme such that the strong-phase difference remains approximately constant within each bin. Large variations in acceptance efficiency within each bin could substantially modify the effective values of the strong phases thus introducing a bias in the determination of mixing and CP-violating parameters. Due to charge detection asymmetries between K^+ and K^-, the Dalitz acceptance can become asymmetric with respect to the principal bisector. This effect is expected to be small, thus a symmetric efficiency model is assumed with $\epsilon(m^2_+, m^2_-) = \epsilon(m^2_-, m^2_+)$. As fitted quantities are ratios of D^0 with D^0 yields and $\bar{D}^0$ with $\bar{D}^0$ yields on opposite sides of the Dalitz plot, asymmetries due to the soft pion and muon can be ignored.

The Dalitz efficiency variation is determined using a data-driven approach that relies on an amplitude model of the unbiased distribution. A background-subtracted data set is produced using the sPlots [72] technique such that each candidate is assigned a signal weight. The number of candidates in a given Dalitz bin is proportional to the product of the acceptance efficiency, $\epsilon(m^2_+, m^2_-)$, and the square of the absolute magnitude of the decay amplitude. The weighted data can divided by the square of the amplitude obtained from an amplitude model to produce a distribution proportional to the acceptance efficiency. Comparisons between background subtracted data and the amplitude model are shown in Fig. 25. The comparison between background subtracted data and an ampli-

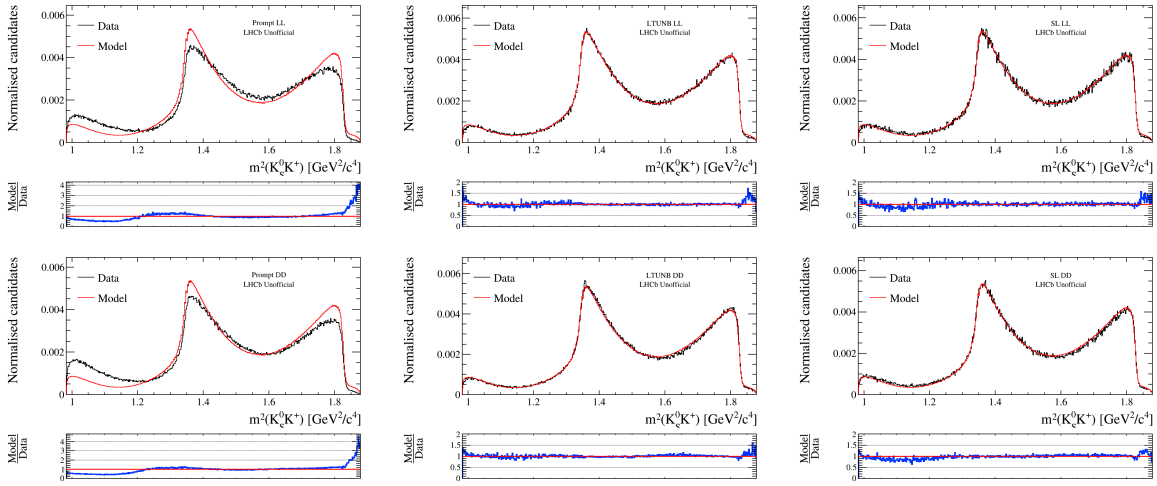


Figure 25: Comparison between background subtracted data and an amplitude model. The plots show m^2_+ projections for the prompt (left), lifetime unbiased prompt (middle) and semileptonic (right) samples. The K^0_S LL category is presented on the top row whilst the K^0_S DD category is presented on the bottom row.

tude model fit by the BaBar collaboration [73], show reasonable agreement for lifetime unbiased and semileptonic samples whilst differences arise in the prompt sample due to Dalitz acceptance effects. It is evident that the trigger induced Dalitz acceptance effects are most severe in the Prompt trigger strategy whilst for the LTUNB and SL samples the amplitude model shows reasonable agreement, suggesting much less severe correlation effects. To produce a smooth distribution, the Dalitz efficiency is fit with a third-order polynomial:

$$\begin{aligned}\epsilon(m^2_+, m^2_-) \propto\ & p_0(m^2_+ + m^2_- - 2m^2_0) + p_1(m^2_+ - m^2_0)(m^2_- - m^2_0) \\ +\ & p_2((m^2_+ - m^2_0)^2 + (m^2_- - m^2_0)^2),\end{aligned} \tag{65}$$

where $m^2_0 = m^2(D^0) - m^2(K^0_S)$. The obtained efficiency distributions are shown in Fig. 26. While the variation of the Dalitz efficiency is quite large for the prompt sample, particularly in the corners of phase-space, variation is much reduced when restricted to a given bin. Such variations may introduce limited biases on the final measurement and should be studied as a potential source of systematic uncertainty.

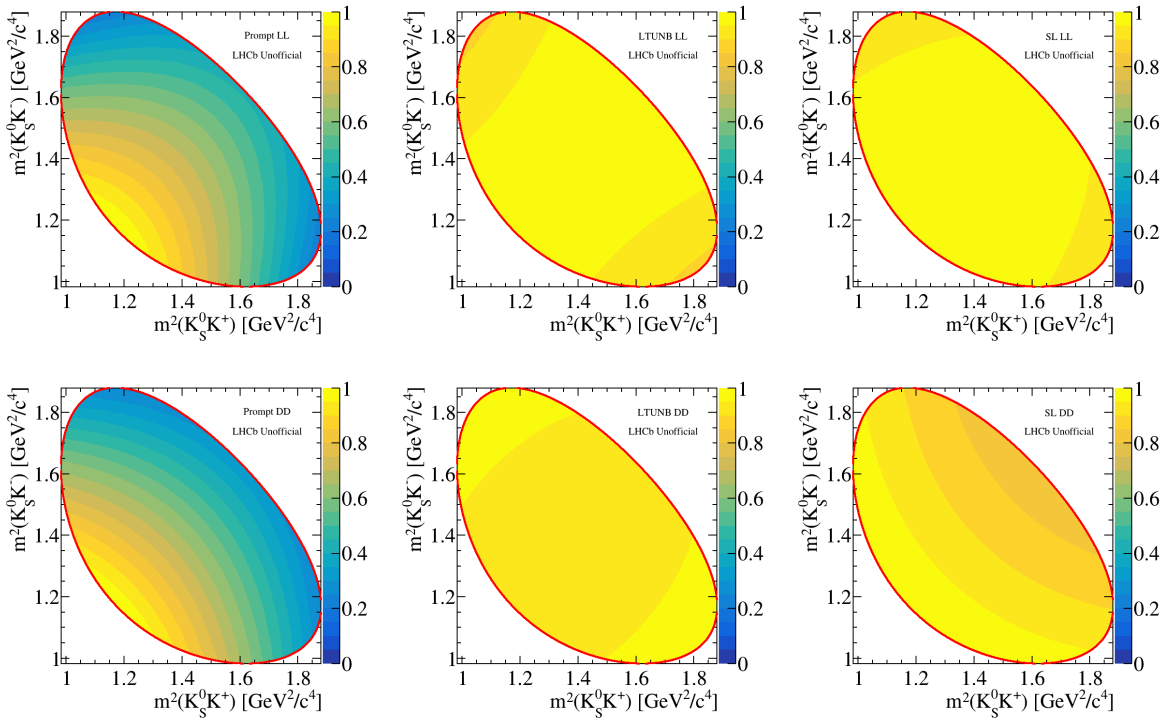


Figure 26: Plots showing the calculated dalitz efficiency relative to a maximum value for the prompt (left), lifetime unbiased prompt (middle) and semileptonic (right) samples. The K^0_S LL category is presented on the top row whilst the K^0_S DD category is presented on the bottom row.

4.10 Correlations between decay-time and Dalitz plot efficiencies

The bin-flip method relies on the assumption that experimentally induced correlations between the decay-time and Dalitz coordinates are negligible. This approach allows for an integration over Dalitz and decay-time bins as well as for decay-time independent coefficients, r_b and X_b, to be determined. Due to stringent selection requirements on the impact parameter of final-state kaon tracks in the software trigger, correlations manifest themselves between the invariant mass of the (K^+K^-) system and the D^0 decay-time. This can be directly observed in the data since in the absence of such correlations the decay-time distribution would be identical across phase-space with small contributions due to neutral-meson mixing.

In addition to Dalitz coordinates, two-dimensional phase-space can be described using a set of "rectangular" Dalitz variables. These variables are $m^2_{K^+K^-}$, the two-body invariant mass of the final state kaons as well as $\cos(\theta_{KK})$. The latter is defined as the cosine of the helicity angle between the K^+ and (K^+K^-) in the (K^+K^-) rest frame. Independent decay-time or Dalitz efficiency variations do not need to be removed since such contributions are expected to cancel when forming a ratio. If the efficiency variation as a function of $(m^2(K^+K^-), t)$ and $(\cos(\theta_{KK}), t)$ is known, the data can be corrected via a candidate-by-candidate weight corresponding to the inverse of the efficiency at the given $(m^2(K^+K^-), t)$ or $(\cos(\theta_{KK}), t)$ coordinate.

The procedure to create an acceptance efficiency map in the $(m^2(K^+K^-), t)$ or $(\cos(\theta_{KK}), t)$ plane is as follows. Each of the six samples, production mode and K^0_S category, is partitioned into ten equally populated decay-time, invariant mass and helicity angle regions (bins). The boundaries of these regions are determined using background-subtracted data. An optimisation procedure is then conducted in order to obtain the two dimensional binning for the correction map. The invariant mass of the two kaons is split into regions such that the bin boundaries are equally spaced within certain intervals. The specification of the binning is provided in Table 10. The helicity angle distribution is divided into twenty equally spaced bins between zero and one. The decay-time boundaries

Table 10: Configuration of the $m^2(KK)$ bins used in the correction map. The boundaries are selected such that each interval is partitioned into a specified number of equally spaced bins.

Region	Mass Interval $[(\text{GeV}/c^2)^2]$	Bins
1	$[\min(m^2(KK)),\ 1.02]$	3
2	$[1.02,\ 1.06]$	15
3	$[1.06,\ 1.2]$	8
4	$[1.2,\ \max(m^2(KK))]$	4

of the correction map are determined dynamically using a reduction algorithm which ensures that for each decay-time region, the corresponding invariant mass or helicity angle bins contain a background-subtracted signal yield above a minimum threshold of 250 signal candidates. As such, the decay-time binning varies for each of the rectangular coordinates. For each "rectangular" coordinate bin i and decay-time bin j the quantity:

$$\epsilon_{ij} = \frac{n_{ij}}{\sum_j n_{ij}} \Bigg/ \frac{n_j}{\sum_j n_j}, \tag{66}$$

is calculated using the observed background subtracted signal yield, n_{ij}. The numerator corresponds to the binned decay-time density for the (i, j) region, while the denominator corresponds to the binned decay-time density averaged over the entire Dalitz plane. The obtained distribution is smoothed using billinear interpolation between bin centers. Acceptance efficiency effects are most pronounced in the DD samples and, if not properly accounted for, can lead to significant biases in the measurement of the mixing parameters. In a uniform acceptance scenario, the plots shown on the left in Figs. 27–32 would appear as horizontal lines at a constant fractional yield. Given that equally populated bins are used in this demonstration, one would expect all lines to lie at a fractional yield of 0.1 (10%). The individual lines represent the fractional signal yield in each decay-time bin across slices of invariant mass or helicity angle. To correct for the acceptance effects, each candidate is weighted by the inverse of the efficiency at its corresponding $(m^2(K^+K^-), t)$ or $(\cos(\theta_{KK}), t)$ coordinate. These weights are applied sequentially, with the $(m^2(K^+K^-), t)$ plane considered first. Once this effect is accounted for, the correction map for the $(\cos(\theta_{KK}), t)$ plane is constructed.

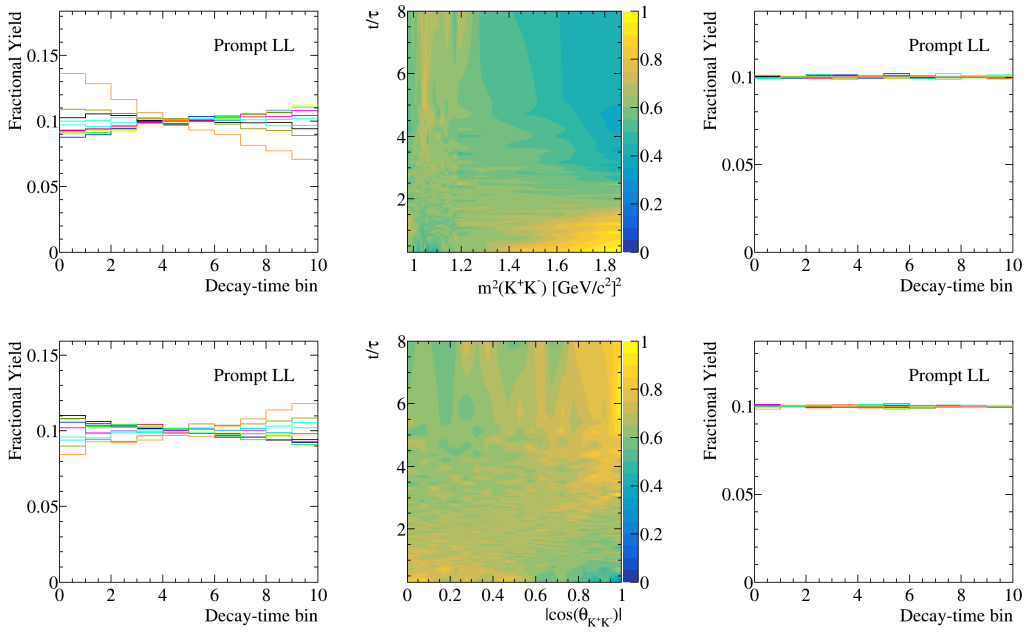


Figure 27: Plots showing fractional yields prior to correction on the left, the correlation map is shown in the middle and the corrected fractional yields are shown on the right for the Prompt LL sample. Each line corresponds to a different m^2_{KK} or $\cos(\theta_{KK})$ bin.

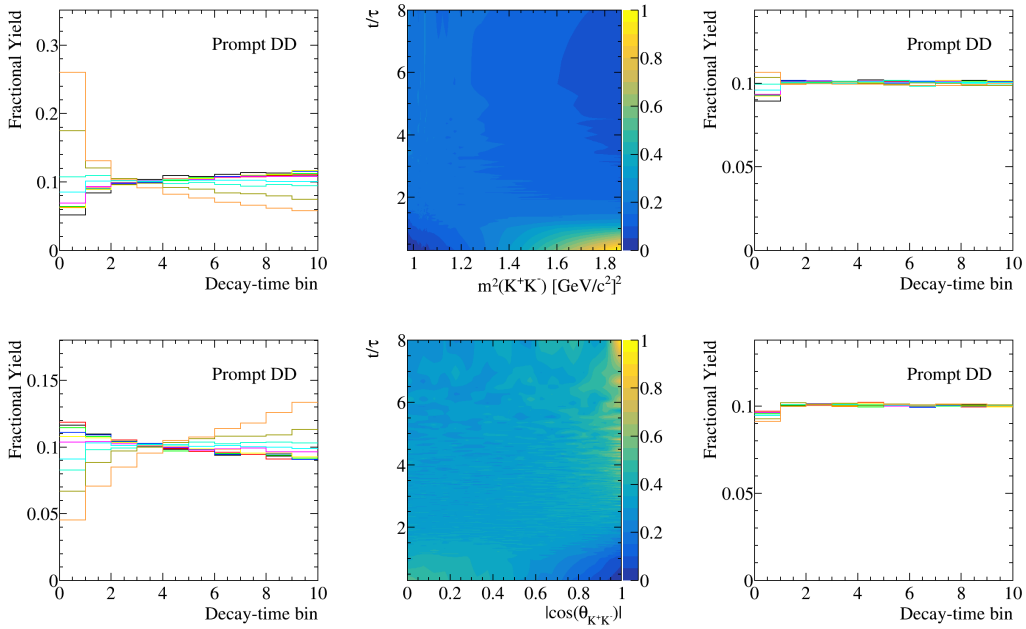


Figure 28: Plots showing fractional yields prior to correction on the left, the correlation map is shown in the middle and the corrected fractional yields are shown on the right for the Prompt DD sample. Each line corresponds to a different m^2_{KK} or $\cos(\theta_{KK})$ bin.

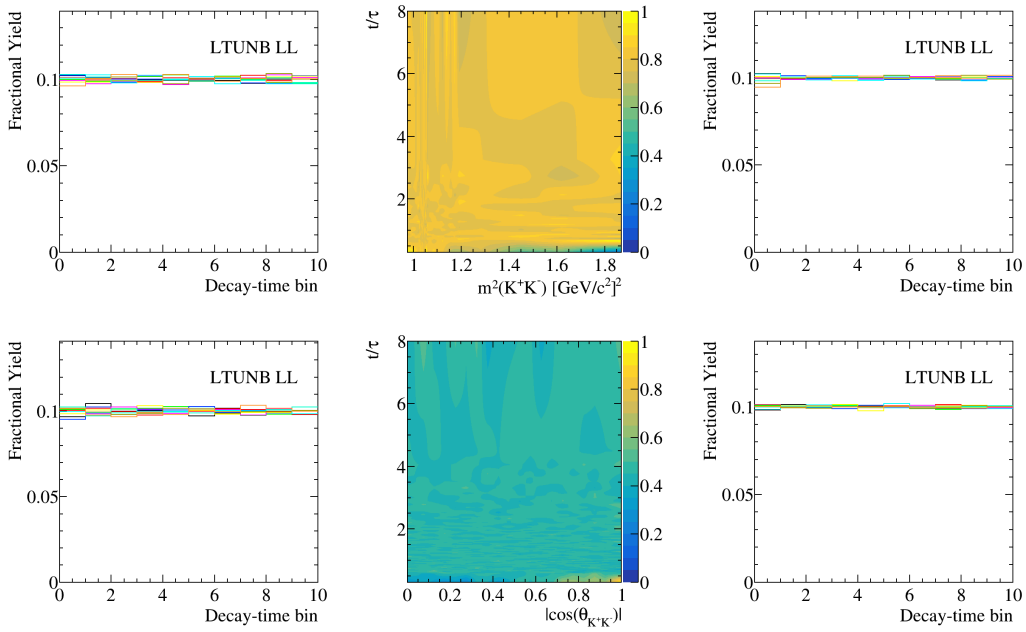


Figure 29: Plots showing fractional yields prior to correction on the left, the correlation map is shown in the middle and the corrected fractional yields are shown on the right for the LTUNB LL sample. Each line corresponds to a different m^2_{KK} or $\cos(\theta_{KK})$ bin.

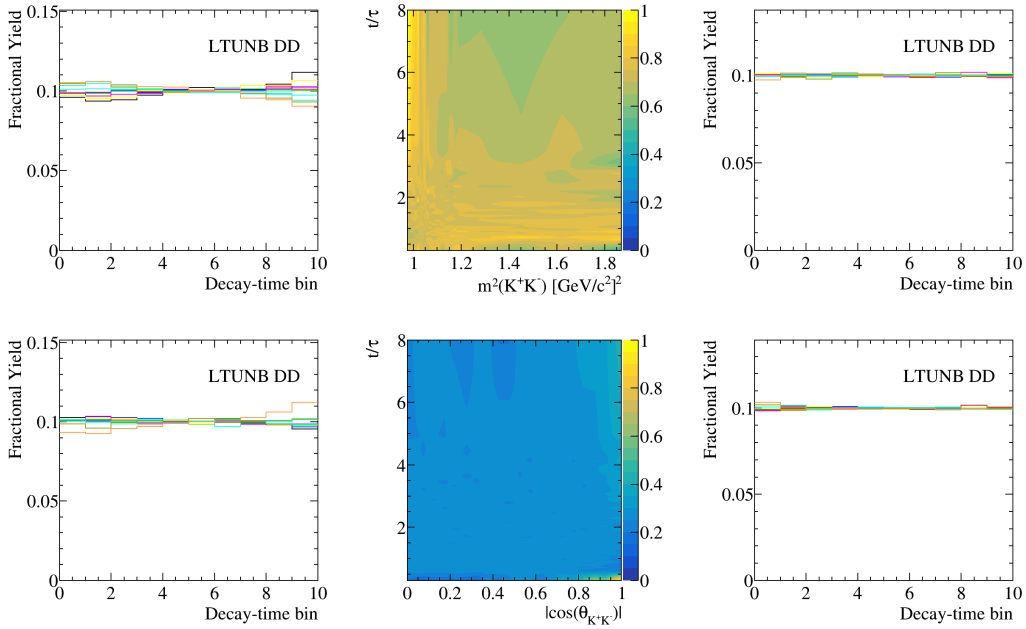


Figure 30: Plots showing fractional yields prior to correction on the left, the correlation map is shown in the middle and the corrected fractional yields are shown on the right for the LTUNB DD sample. Each line corresponds to a different m^2_{KK} or $\cos(\theta_{KK})$ bin.

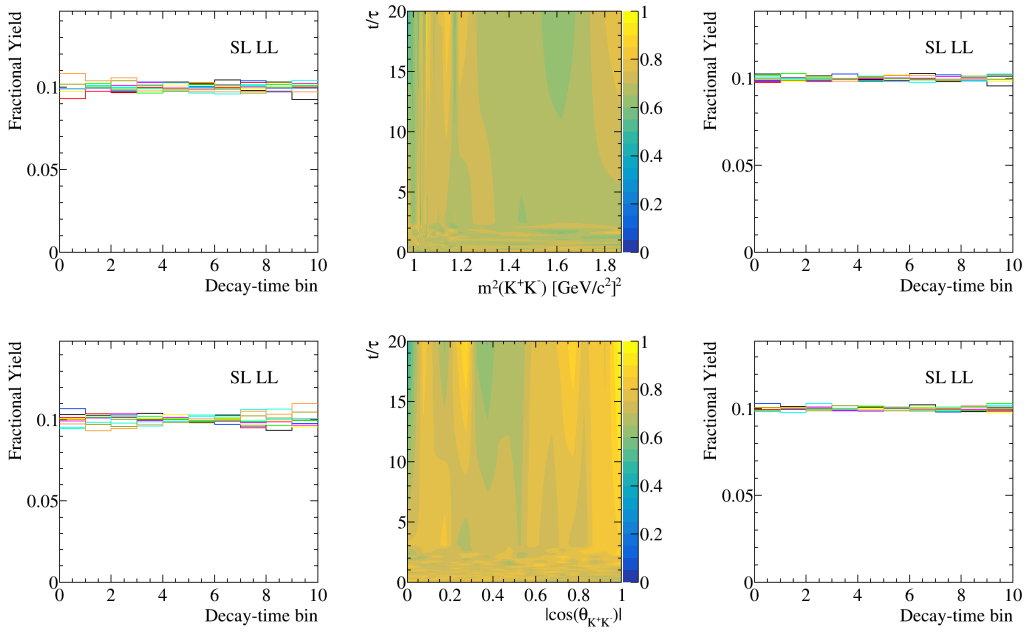


Figure 31: Plots showing fractional yields prior to correction on the left, the correlation map is shown in the middle and the corrected fractional yields are shown on the right for the semileptonic LL sample. Each line corresponds to a different m^2_{KK} or $\cos(\theta_{KK})$ bin.

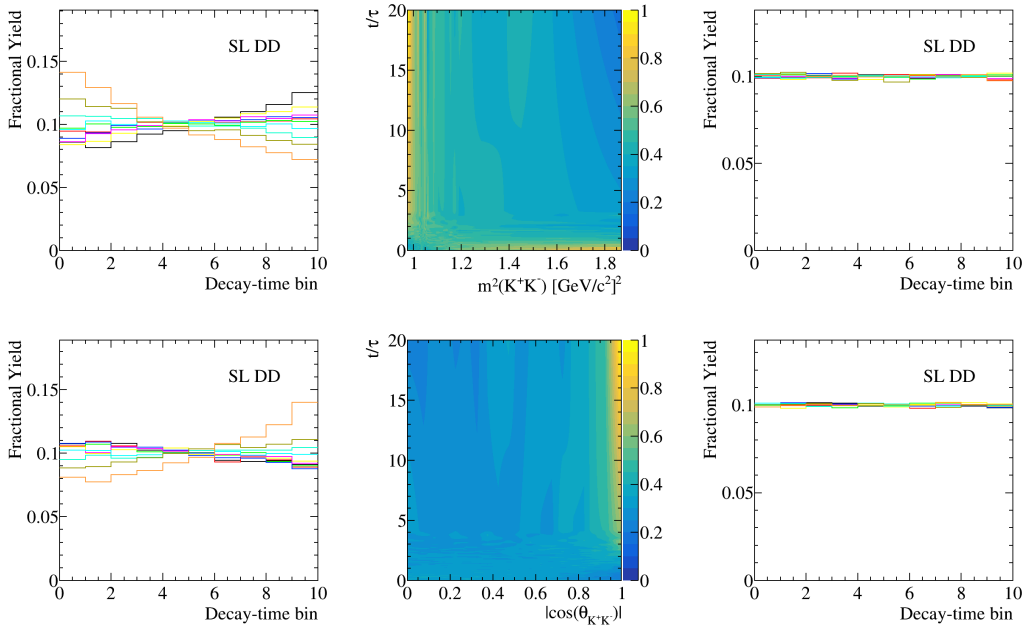


Figure 32: Plots showing fractional yields prior to correction on the left, the correlation map is shown in the middle and the corrected fractional yields are shown on the right for the semileptonic DD sample. Each line corresponds to a different m^2_{KK} or $\cos(\theta_{KK})$ bin.

5 Fits to data

In the bin-flip fit, the data are divided into subsamples according to trigger strategy, K^0_S decay, D^0 meson flavour, position on the Dalitz plot and D^0 decay-time. In this analysis the bin-flip fit is performed using two Dalitz bins and ten lifetime bins.

5.1 Signal yield extraction

In order to extract signal yields in each Dalitz and decay-time bin, binned fits are performed to the Δm and $m(K^0K^+K^-)$ masses for the Prompt/LTUNB and semileptonic samples respectively. Prior to fitting, each candidate is weighted using the correction weight obtained from the $m^2(KK)$ correlation map. As stated previously, the signal component is parameterised as a combination of a core JohnsonSU and a floating Gaussian component, whilst the background shape is an empirical threshold function for the Prompt/LTUNB samples and a second-order Chebyshev polynomial for the semileptonic sample. The signal-shape parameters are shared between candidates populating the positive and negative Dalitz plot bins whilst the background shape parameters are fit independently. The signal shape parameters are fixed to those obtained using a phase-space and decay-time integrated fit. Only the means of the signal components are allowed to float in the yield extraction procedure. Example fits to the LL D^0 samples are presented in Fig. 33. Event yields for the $\bar{D}^0$ flavour are extracted separately, following the same procedure.

5.2 Determination of $\langle t \rangle$ and $\langle t^2 \rangle$

In order to perform the final measurement, the average values of the decay-time, $\langle t \rangle$, and squared decay-time, $\langle t^2 \rangle$, must be calculated. In this calculation samples are restricted to the lower region of the Dalitz plot ($m^2_+ > m^2_-$) since this region is enriched with D^0 mesons that have not undergone mixing. The average decay-time and squared decay-time are then obtained using a background subtracted sample of D^0 mesons such that

$$\langle t_j \rangle = \frac{\sum_i w_i t_i}{\sum_i w_i} \text{ and } \langle t^2_j \rangle = \frac{\sum_i w_i t^2_i}{\sum_i w_i} \tag{67}$$

where the sum goes over all candidates populating the decay-time bin j and w_i is the weight assigned to the candidate i with decay time t_i. The weight, w_i, is a product of the background subtraction weight and the correction weight obtained from the correlation removal procedure. Example fits used to obtain background-subtracted candidates are presented in Fig. 34.

5.3 Determination of mixing parameters

The mixing parameters are determined using a least-squares fit that compares the decay-time evolution of signal yields observed in the Dalitz plot bins $-i$ and i, along with their

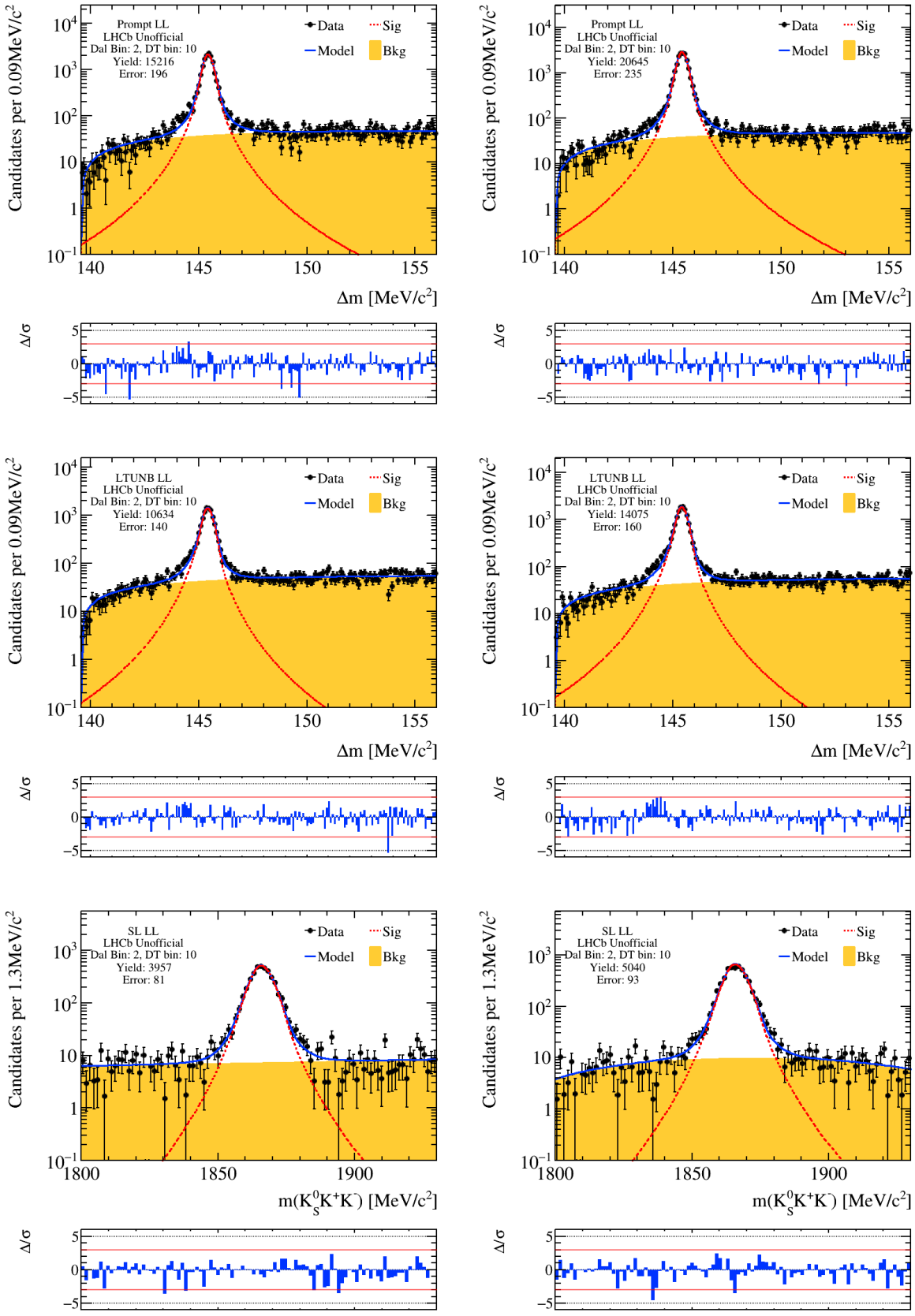


Figure 33: Projections of simultaneous fits to the positive (left) and negative (right) bin for the second Dalitz bin (dominated by phi band) and highest lifetime bin for the Prompt LL (top), LTUNB LL (middle) and semileptonic LL (bottom) samples.

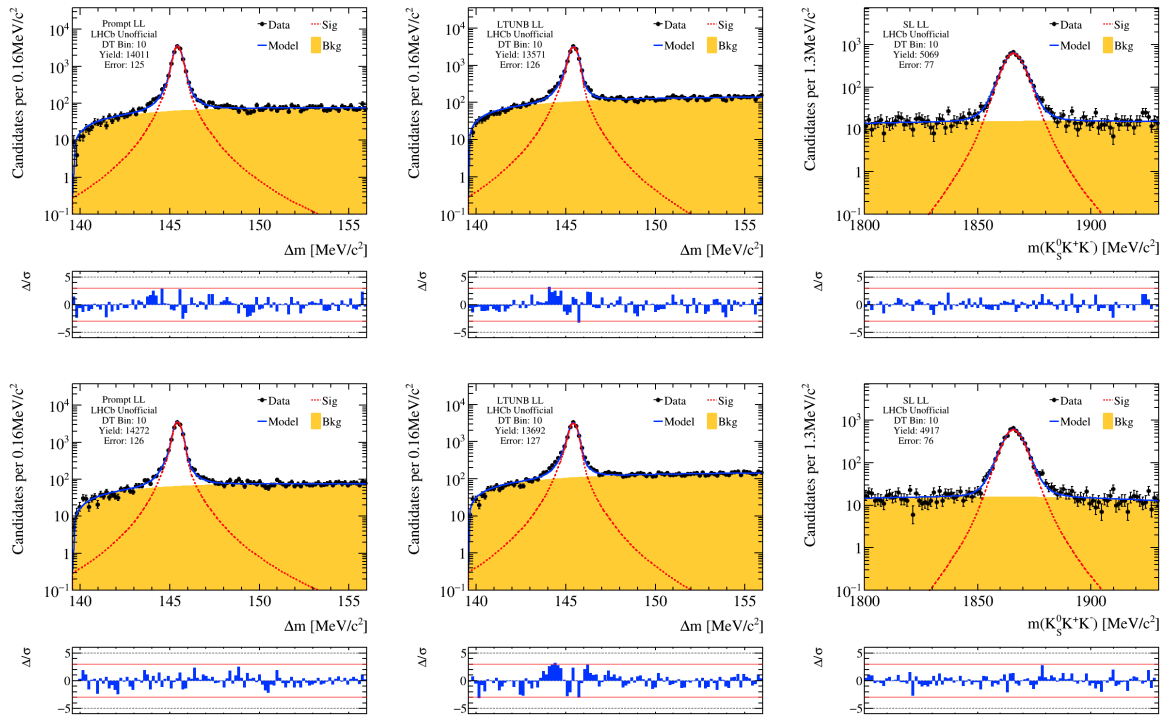


Figure 34: Fits used to obtain background-subtracted candidates for the D^0 (top) and $\bar{D}^0$ (bottom) mesons in the highest lifetime bin the Prompt LL (left), LTUNB LL (middle) and semileptonic LL (right) samples.

uncertainties, as determined from the previous fits, with the expected values reported in Equation 56:

$$\chi^2 = \sum_{i,j} \left[\frac{(N^+_{-ij} - N^+_{ij} R^+_{ij})^2}{(\sigma^2_{-ij})^2 + (\sigma_{ij} R^+_{ij})^2} + \frac{(N^-_{-ij} - N^-_{ij} R^-_{ij})^2}{(\bar{\sigma}^2_{-ij})^2 + (\bar{\sigma}_{ij} R^-_{ij})^2} \right] + \chi^2_X \text{ , with} \tag{68}$$

$$\chi^2_X = \sum_{i,k} [X_i^{BESIII} - X_i](V^{-1}_{BESIII})_{ik}[X_k^{BESIII} - X_k], \tag{69}$$

which is simultaneously applied to all Dalitz plot bins, i, and decay time bins, j. A penalty term, χ^2_X, is introduced to constrain the strong phases (X_b) and utilises auxiliary values, X_b^{BESIII}, measured by the BESIII collaboration. The V_{BESIII} term corresponds to the covariance matrix and is given by the sum of the statistical and systematic covariance matrices. The central values have been provided in Section 2.8 of this thesis. In the case of CP conservation, $\Delta z = 0$, the theoretical prediction for the ratio of yields in each bin becomes:

$$R^{\pm}_{ij} \approx \frac{r_i[1 + \frac{1}{4}\langle t^2\rangle_j \,\mathrm{Re}(z^2_{CP})] + \frac{1}{4}\langle t^2\rangle_j |z_{CP}|^2 + \langle t\rangle_j \sqrt{r_i}\,\mathrm{Re}(X_i^\dagger(z_{CP}))}{1 + \frac{1}{4}\langle t^2\rangle_j \,\mathrm{Re}(z^2_{CP}) + r_i \frac{1}{4}\langle t^2\rangle_j |z_{CP}|^2 + \langle t\rangle_j \sqrt{r_i}\,\mathrm{Re}(X_i(z_{CP}))}, \tag{70}$$

where $x_{CP} = -\,\mathrm{Im}(z_{CP})$ and $y_{CP} = -\,\mathrm{Re}(z_{CP})$. This is obtained by setting Δz to zero in Equation 55. In order to measure the mixing parameters, initially the mixing parameters are fixed to the world average values whilst the strong phases are fixed to the BESIII central values. In the first instance only the r_i parameters are allowed to float. Gradually

the strong phases are released under a Gaussian constraint and eventually the mixing parameters are allowed to float freely in the final stage.

5.4 Results

The measured mixing parameters are presented in Table. 11. A fit is performed to each individual sample separately, then the LL samples are considered simultaneously. The fits to the Prompt DD and SL DD samples did not converge.

Table 11: Measured mixing parameters for each trigger category.

Sample	x [%]	y [%]	Prob(χ^2/ndof)
Prompt LL	8.9 ± 4.1	1.4 ± 3.1	0.61
Prompt DD	Fit did not converge		
LTUNB LL	0.046 ± 0.67	0.96 ± 2.2	0.01
LTUNB DD	$1.4 \pm .3$	1.0 ± 3.5	0.89
SL LL	2.3 ± 1.9	5.9 ± 5.1	0.13
SL DD	Fit did not converge		
Prompt + LTUNB LL	2.9 ± 1.4	5.4 ± 3.1	0.00049

The fit projections are presented in Fig. 36 for the simultaneous fit to the Prompt and LTUNB LL samples. It is evident that for the LTUNB DD sample the ratios in the second Dalitz bin (right) trend in the opposite direction. This is due to the severe correlations introduced by the selection procedure. The contour plot for the mixing parameters obtained from the simultaneous fit to the Prompt and LTUNB samples is presented in Fig 35. It can be seen that the results are consistent with the world average measurement. Although the measurement of the charm mixing parameters x and y is not competitive with the world average, the analysis has potential to improve the uncertainty on the strong phases.

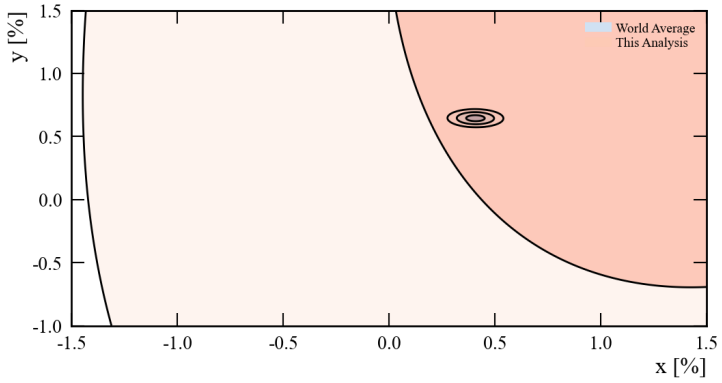


Figure 35: Contour plot of the mixing parameters. The world average is presented in blue whilst the red corresponds to this analysis.

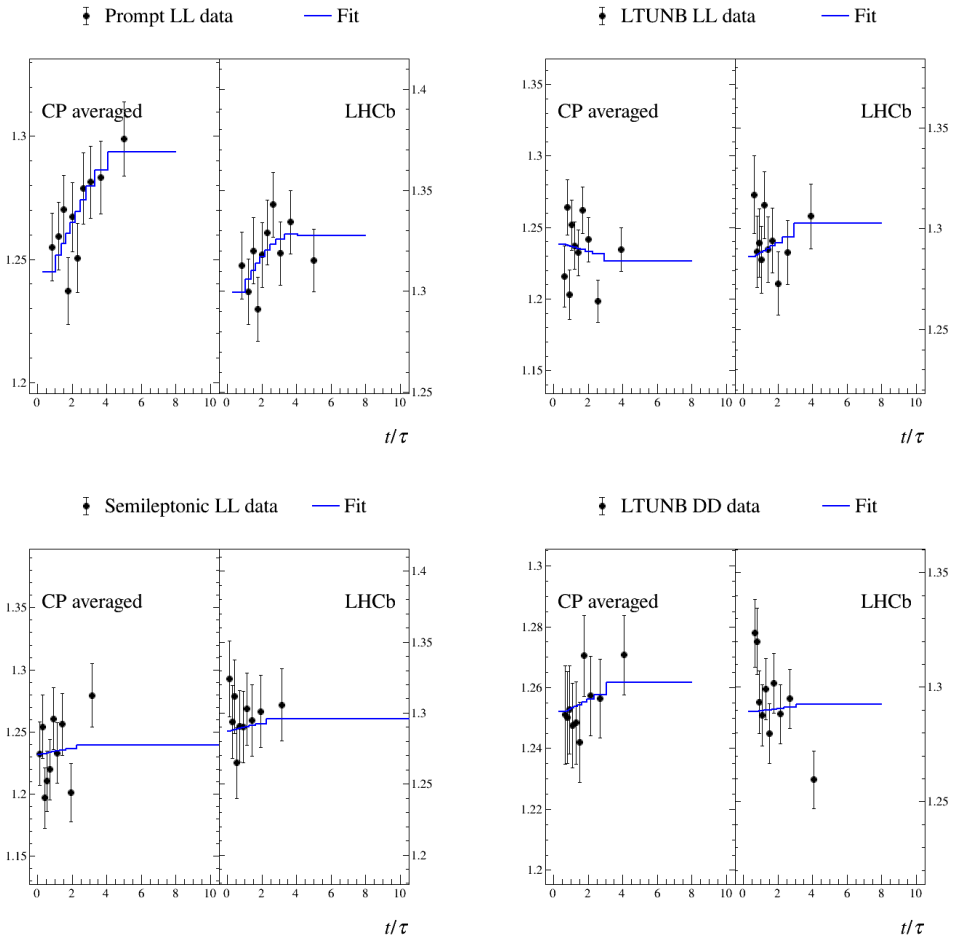


Figure 36: Fit projections for each of the trigger categories. The CP averaged ratios of fractional yields are shown on the y-axis whilst the decay-time bins are shown on the x-axis. The first Dalitz bin is presented on the left of each plot whilst the second Dalitz bin is presented on the right. The ϕ resonance resides in the second Dalitz bin.

6 Future work

The results of this analysis suggest that a measurement of charm mixing parameters is feasible using the $D^0 \to K^0_S K^+ K^-$ decay mode, however further work is necessary in order to reach a complete result. As such systematic uncertainties must be studied and additional improvements to the analysis can be performed.

6.1 Systematic uncertainties

The first systematic uncertainty arises due to the choice of signal shape. In particular since all of the parameters are fixed from a global fit, this only allows for signal and background yields to float in each bin. This can cause biases especially as the Δm and $m(K^0_S K^+ K^-)$ distributions can vary as a function of D^0 lifetime and position on the Dalitz plot. In this analysis a simple systematic uncertainty is evaluated by performing the fitting procedure using a background-subtracted sample obtained from a phase-space and decay-time integrated fit. The measured central values for the mixing parameters

are then subtracted from the previously obtained values in order to assign a systematic. Using this procedure the final measured values for the mixing parameters are:

$$\begin{aligned} x &= (2.9 \pm 1.4 \pm 0.1)\% \\ y &= (5.4 \pm 3.1 \pm 1.0)\% \end{aligned} \tag{71}$$

where the first uncertainty is statistical and the second is systematic due to choice of signal shape. In order to evaluate this systematic in a more rigorous manner, the procedure should be repeated by instead using a different signal and background parameterisation. For example this could involve the introduction of another Gaussian function as part of the core component. The current world average values for x and y can be found on page 13.

In the application of the bin-flip method to Prompt $D^0 \to K^0_S\pi^+\pi^-$ decays, the contribution of semileptonic decays misidentified as Prompt production was found to be a leading source of systematic uncertainty in the measurement of the x mixing parameter [44]. Therefore this type of contamination must be considered in a future measurement for the $D^0 \to K^0_S K^+ K^-$ decay. A significant fraction of the selected signal Prompt and LTUNB candidates originates from the decays of b-hadrons. The imposed selection on the IPχ^2 of the D^0, required to not exceed 9, reduces the total contribution of this component to $\mathcal{O}(1)\%$, with the relative contribution increasing as a function of the D^0 decay-time. Particularly, the measured decay-time of the signal candidates will be systematically larger in comparison to the genuine decay-time as the observed lifetime is calculated with respect to the PV, which is unlikely to coincide with the D^0 production vertex. As such, the presence of this component will systematically bias the fit result by altering the lifetime in each decay-time bin. In a future study this effect would be accounted for by introducing a secondary component to the mixing fit minimisation function or assigned as a systematic uncertainty.

In order to study this contamination, selective candidates are reconstructed by combining a D^{*+} with a muon from the same event in order to form $B^0 \to D^{*+}\mu^- X$ decays. Candidates are preselected as outlined previously with a few additional requirements which are presented in Table 12. Candidates that satisfy this initial selection are then

Table 12: Selection of $B^0 \to D^{*+}\mu^- X$ decays.

Particle	Variable	Requirement
μ	Transverse momentum	> 1000 MeV/c
	IP χ^2 with respect to PV	> 4
	ProbNNmu	> 0.5
B	Mass	$\in [3.0, 5.1]$ GeV/c^2
	Vertex-fit χ^2	< 25

matched to Prompt/LTUNB candidates. For this study, the IPχ^2 selection on the D^0 as well as all DTF quality requirements are removed. To extract the secondary contamination, a template fit is performed to the log of the D^0 IPχ^2 in bins of D^0 decay-time as is as follows:

- Candidates are separated into signal and background regions by partitioning the Δm distribution. The signal region is defined as $\Delta m \in [142, 148]$ MeV/c^2 and the background region is defined as $\Delta m \in [149, 156]$ MeV/c^2.
- To subtract the background, the sideband of the Δm distribution is scaled to equal the total number of background events within the signal region. This scale factor is obtained from a fit to the Δm distribution.
- Two 2D histograms (decay-time vs IPχ^2) are filled, one for the signal and one for the background. Then, the scaled background histogram is subtracted from the signal. This procedure is performed for both the Prompt and LTUNB and respective selective secondary candidates.
- The prompt/LTUNB templates are taken from projections of the lowest decay-time bin.
- A template fit is then performed in all of the other bins to extract the secondary fraction by using the obtained normalisation.

Example template fits obtained for the highest decay-time bins are provided in Fig. 37 and the distributions of the secondary fractions as a function of decay-time are provided in Fig. 38. It can be seen that the secondary fraction increases as a function of the D^0 lifetime.

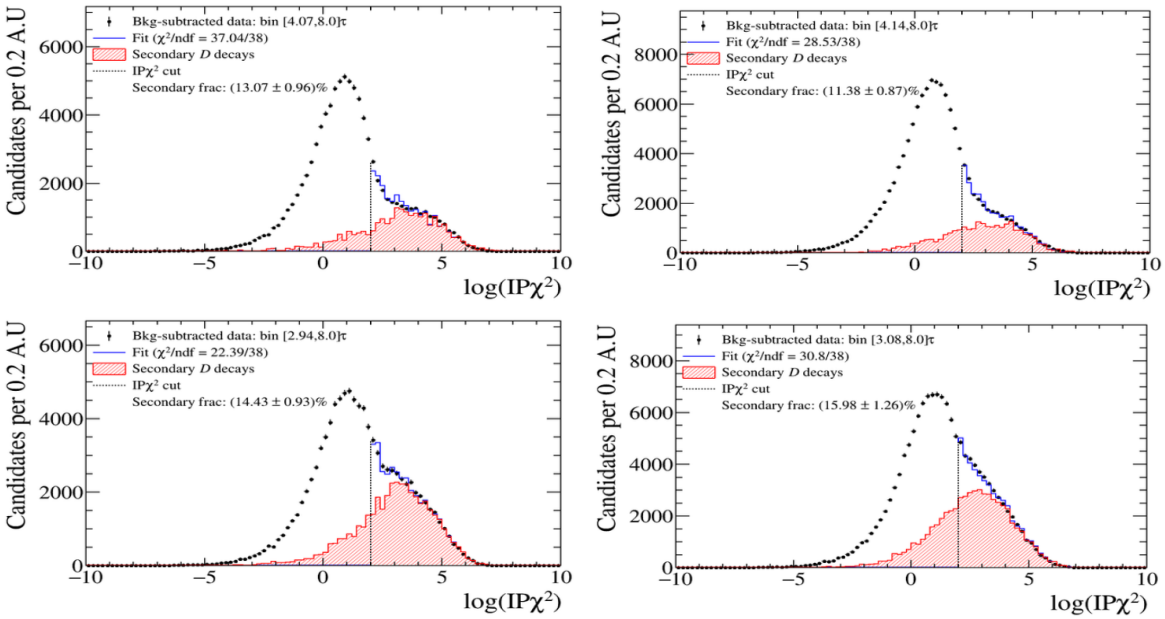


Figure 37: Plots showing secondary contamination in the highest decay-time bin for the Prompt LL (top left), Prompt DD (top right), LTUNB LL (bottom left) and LTUNB DD (bottom right) samples.

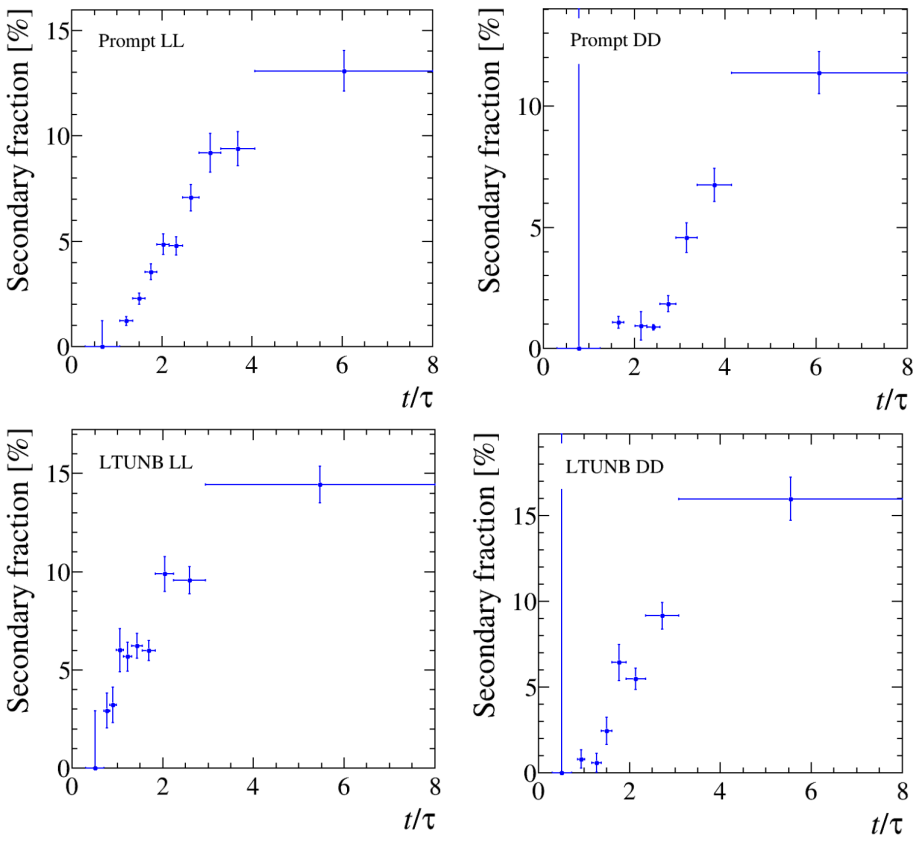


Figure 38: Plots showing secondary contamination as a function of decay-time for the Prompt LL (top left), Prompt DD (top right), LTUNB LL (bottom left) and LTUNB DD (bottom right) samples.

6.2 Future improvements

In order to improve the measured mixing parameters several steps can be taken. Firstly the correlation removal procedure should be split by the HLT1 trigger type for the prompt and ltunb samples. This is particuarly important since the HLT1 selections may introduce correlations which can only be accounted for using an independent consideration. In particular, the correlations are most severe for the DD samples where only the final-state kaons are reconstructed as long tracks. Additionally the correlation removal procedure should be studied for each data taking year and magnet polarity. The presented results account only for the $m^2(KK)$ correlations, the cosine of the helicity angles should be considered in the future. Additionally, due to the presence of secondaries in the Prompt and LTUNB samples it may be necessary to account for this contribution in the yield extraction procedure.

7 Conclusion

A sample of $D^0 \to K^0_S K^+ K^-$ decays has been selected using Run II data collected by the LHCb experiment in three trigger strategies. A total of approximately three million and seven hundred thousand candidates has been found. A deficit in the prompt sample with

respect to expectation has been understood. This analysis shows that a measurement of mixing parameters in $D^0 \to K^0_S K^+ K^-$ is feasible. Although the measurement is not competitive in comparison to $D^0 \to K^0_S \pi^+ \pi^-$, it is still important to measure mixing parameters in charm using an alternative decay mode. Further work is necessary to fully account for systematic uncertainties in order to obtain a complete measurement.

References

[1] X. Fan, T.G. Myers, B.A.D. Sukra, and G. Gabrielse. Measurement of the electron magnetic moment. *Physical Review Letters*, 130(7).

[2] F. Abe et al. Observation of top quark production in $\overline{p}p$ collisions with the collider detector at fermilab. *Phys. Rev. Lett.*, 74:2626–2631, Apr 1995.

[3] S. Abachi et al. Observation of the top quark. *Phys. Rev. Lett.*, 74:2632–2637, Apr 1995.

[4] K. Kodama et al. Observation of tau neutrino interactions. *Physics Letters B*, 504(3):218–224, 2001.

[5] G. Aad et al. Observation of a new particle in the search for the standard model higgs boson with the atlas detector at the lhc. *Physics Letters B*, 716(1):1–29, 2012.

[6] S. Chatrchyan et al. Observation of a new boson at a mass of 125 gev with the cms experiment at the lhc. *Physics Letters B*, 716(1):30–61, 2012.

[7] Virginia Trimble. Existence and nature of dark matter in the universe. *Annual Review of Astronomy and Astrophysics*, 25(Volume 25, 1987):425–472, 1987.

[8] Laurent Canetti, Marco Drewes, and Mikhail Shaposhnikov. Matter and antimatter in the universe. *New Journal of Physics*, 14(9):095012, sep 2012.

[9] L. Wolfenstein. *$D^0 - \overline{D}^0$ mixing. Physics Letters B*, 164(1):170 – 172, 1985.

[10] B.R Holstein J.F Donoghue, E. Golowich and J. Trampetić. *Dispersive effects in $D^0 - \overline{D}^0$ mixing. Phys. Rev. D*, 33:179–183, 1986.

[11] Y. Nir G. Isidori and G.Perez. *Flavor Physics Constraints for Physics Beyond the Standard Model. Ann. Rev. Nucl. Part. Sci.*, 60:355, 2010. arXiv:1002.0900.

[12] S. Pakvasa E. Golowich and A. Petrov. *New Physics Contributions to the Lifetime Difference in $D^0 - \overline{D}^0$ Mixing. Phys. Rev. Lett.*, 98:181801, Apr 2007.

[13] S. Pakvasa E. Golowich, J. Hewett and A. Petrov. *Implications of $D^0 - \overline{D}^0$ mixing for new physics. Phys. Rev. D*, 76:095009, Nov 2007.

[14] M. Bobrowski, A. Lenz, J. Riedl, and J. Rohrwild. *How large can the SM contribution to CP violation in $D^0 - \overline{D}^0$ mixing be? JHEP 03 (2010) 009.*

[15] Ikaros I Bigi, Monika Blanke, Andrzej J Buras, and Stefan Recksiegel. *CP violation in $D^0 - \overline{D}^0$ oscillations: general considerations and applications to the Littlest Higgs model with T-parity. Journal of High Energy Physics*, 2009(07):097–097, jul 2009.

[16] M. Tanabashi et al. *Review of Particle Physics. Phys. Rev. D*, 98:030001, Aug 2018.

[17] H. Albrecht et al. *Observation of $B^0 - \bar{B}^0$ mixing. Physics Letters B*, 192(1):245, 1987.

[18] A. Abulencia et al. *Observation of $B_s^0 - \bar{B}_s^0$ oscillations. Phys. Rev. Lett.*, 97:242003, 2006.

[19] R. Aaij et al. *Observation of $D^0 - \overline{D}^0$ oscillations. Phys. Rev. Lett.*, 110(10):101802, 2013.

[20] R. Aaij et al. *Observation of CP violation in charm decays. Phys. Rev. Lett.*, 122(21):211803, 2019.

[21] J. Libby et al. *Model-independent determination of the strong-phase difference between D^0 and $\bar{D}^0 \to K^0_{S,L} h^+ h^-$ ($h = \pi, K$) and its impact on the measurement of the CKM angle γ/ϕ_3. Phys. Rev.*, D82:112006, 2010.

[22] Medina Ablikim et al. *Improved model-independent determination of the strong-phase difference between D^0 and $\bar{D}^0 \to K^0_{\rm S,L} K^+ K^-$ decays. Phys. Rev. D*, 102(5):052008, 2020.

[23] R. Aaij et al. *Measurement of the CKM angle γ using $B^\pm \to DK^\pm$ with $D \to K^0_S \pi^+ \pi^-$, $K^0_S K^+ K^-$ decays. JHEP*, 08:176, 2018. [erratum: JHEP10,107(2018)].

[24] Wikipedia. *Standard Model. https://en.wikipedia.org/wiki/Standard_Model*, 2024.

[25] S. Mertens. Direct neutrino mass experiments. *Journal of Physics: Conference Series*, 718(2):022013.

[26] R. Aaij et al. Observation of $j/\psi p$ resonances consistent with pentaquark states in $\Lambda_b^0 \to j/\psi K^- p$ decays. *Phys. Rev. Lett.*, 115:072001, Aug 2015.

[27] Emmy Noether. Invariant variation problems. *Transport Theory and Statistical Physics*, 1(3):186–207, 1971.

[28] Julian S. Schwinger. The theory of quantized fields. i. *Phys. Rev.*, 82:914–927, 1951.

[29] T. D. Lee and C. N. Yang. Question of parity conservation in weak interactions. *Physical Review*, 104:254–258, 1956.

[30] C. S. Wu et al. Experimental test of parity conservation in beta decay. *Physical Review*, 105:1413–1415, 1957.

[31] J. H. Christenson, J. W. Cronin, V. L. Fitch, and R. K. E. M. Evidence for the 2 decay of the k20 meson. *Physical Review Letters*, 13:138–140, 1964.

[32] E. Gabathuler and P. Pavlopoulos. The cplear experiment. *Physics Reports*, 403-404:303–321, 2004.

[33] Andrei D Sakharov. Violation of cp invariance, c asymmetry, and baryon asymmetry of the universe. *Soviet Physics Uspekhi*, 34(5):392, may 1991.

[34] Nicola Cabibbo. Unitary symmetry and leptonic decays. *Phys. Rev. Lett.*, 10:531–533, Jun 1963.

[35] S. L. Glashow, J. Iliopoulos, and L. Maiani. Weak interactions with lepton-hadron symmetry. *Phys. Rev. D*, 2:1285–1292, Oct 1970.

[36] Mark Thomson. *Modern Particle Physics*. Cambridge University Press, 2013.

[37] Makoto Kobayashi and Toshihide Maskawa. *CP-Violation in the Renormalizable Theory of Weak Interaction. Progress of Theoretical Physics*, 49(2):652–657, 02 1973.

[38] Lincoln Wolfenstein. *Parametrization of the Kobayashi-Maskawa Matrix. Phys. Rev. Lett.*, 51:1945–1947, Nov 1983.

[39] LHCb Collaboration. *Simultaneous determination of the CKM angle γ and parameters related to mixing and CP violation in the charm sector*. 2022. LHCb-CONF-2022-003.

[40] CKMfitter Group. *Current status of the standard model CKM fit and constraints on $\Delta F = 2$ new physics. Phys. Rev. D*, 91:073007, 2015.

[41] V. Weisskopf and E. Wigner. *Over the natural line width in the radiation of the harmonious oscillator. Z. Phys.*, 65:18–29, 1930.

[42] R. L. Workman et al. Particle Data Group. *Review of Particle Physics. Prog. Theor. Exp. Phys.*, 2022(8):083C01, 2022.

[43] Y. Amhis et al. Heavy Flavor Averaging Group. *Averages of b-hadron, c-hadron, and τ-lepton properties.* Updated results and plots available at urlhttps://hflav.web.cern.ch.

[44] R. Aaij et al. *Observation of the Mass Difference between Neutral Charm-Meson Eigenstates. Phys. Rev. Lett.*, 127:111801, Sep 2021.

[45] R. Aaij et al. *Observation of CP Violation in Charm Decays. Phys. Rev. Lett.*, 122:211803, May 2019.

[46] R.H. Dalitz. *CXII. On the analysis of τ-meson data and the nature of the τ-meson. The London, Edinburgh, and Dublin Philosophical Magazine and Journal of Science*, 44(357):1068, 1953.

[47] A. Poluektov A. Bondar and V. Vorobiev. *Charm mixing in the model-independent analysis of correlated D^0 $\bar{D}^0$ decays. Phys. Rev.*, D82:034033, 2010.

[48] C. Thomas and G. Wilkinson. *Model-independent $D^0 - \bar{D}^0$ mixing and CP violation studies with $D^0 \to K^0_S\pi^+\pi^-$ and $D^0 \to K^0_S K^+K^-$. JHEP*, 10:185, 2012.

[49] R. Aaij et al. *Model-independent measurement of mixing parameters in $D^0 \to K^0_s\pi^+\pi^-$ decays. JHEP*, 04:033, 2016.

[50] A. Di Canto, J. Garra Ticó, T. Gershon, N. Jurik, M. Martinelli, T. Pilař, S. Stahl, and D. Tonelli. *Novel method for measuring charm-mixing parameters using multi-body decays. Phys. Rev.*, D99(1):012007, 2019.

[51] M. Ablikim et al. *Improved model-independent determination of the strong-phase difference between D^0 and $\overline{D}^0 \to K^0_{S,L}K^+K^-$ decays. Phys. Rev. D*, 102:052008, Sep 2020.

[52] M. Ablikim et al. *Model-independent determination of the relative strong-phase difference between D^0 and $\overline{D}^0 \to K^0_{S,L}\pi^+\pi^-$ and its impact on the measurement of the CKM angle γ/ϕ_3. Phys. Rev. D*, 101:112002, Jun 2020.

[53] E. Mobs. *The CERN accelerator complex - August 2018. Complexe des accélérateurs du CERN - Août 2018*, 2018. General Photo.

[54] Lyndon Evans and Philip Bryant. *LHC Machine. Journal of Instrumentation*, 3(08):S08001, aug 2008.

[55] A.A Alves Jr et al. *The LHCb Detector at the LHC. Journal of Instrumentation*, 3(08):S08005, Aug 2008.

[56] R. Aaij et al. *LHCb Detector Performance. Int. J. Mod. Phys.*, A30(07):1530022, 2015.

[57] Torbjorn Sjostrand, Stephen Mrenna, and Peter Z. Skands. *A Brief Introduction to PYTHIA 8.1. Comput. Phys. Commun.*, 178:852–867, 2008.

[58] I Belyaev et al. *Handling of the generation of primary events in Gauss, the LHCb simulation framework. Journal of Physics: Conference Series*, 331(3):032047, dec 2011.

[59] David J. Lange. *The EvtGen particle decay simulation package. Nuclear Instruments and Methods in Physics Research Section A: Accelerators, Spectrometers, Detectors and Associated Equipment*, 462(1):152 – 155, 2001. BEAUTY2000, Proceedings of the 7th Int. Conf. on B-Physics at Hadron Machines.

[60] P. Golonka and Z. Was. *PHOTOS Monte Carlo: a precision tool for QED correctionsin Z and W decays. Eur.Phys.J. C*, 45(1):97 – 107, 2006.

[61] S. Agostinelli et al. *Geant4—a simulation toolkit. Nuclear Instruments and Methods in Physics Research Section A: Accelerators, Spectrometers, Detectors and Associated Equipment*, 506(3):250 – 303, 2003.

[62] M Clemencic, G Corti, S Easo, C R Jones, S Miglioranzi, M Pappagallo, and P Robbe and. *The LHCb Simulation Application, Gauss: Design, Evolution and Experience. Journal of Physics: Conference Series*, 331(3):032023, dec 2011.

[63] LHCb collaboration. *Track types for the LHCb Run I and II.* https://twiki.cern.ch/twiki/pub/LHCb/ConferencePlots/trackTypesRunIAndII.pdf.

[64] R. Aaij et al. *Design and performance of the LHCb trigger and full real-time reconstruction in Run 2 of the LHC. Journal of Instrumentation*, 14(04):P04013, apr 2019.

[65] R. Aaij et al. *Tesla: An application for real-time data analysis in High Energy Physics. Computer Physics Communications*, 208:35–42, 2016.

[66] Sean Benson, Vladimir Gligorov, Mika Anton Vesterinen, and John Michael Williams. *The LHCb Turbo Stream. Journal of Physics: Conference Series*, 664(8):082004, dec 2015.

[67] Bernard Aubert et al. *Improved measurement of the CKM angle γ in $B^{\mp} \to D^{(*)}K^{(*\mp)}$ decays with a Dalitz plot analysis of D decays to $K^0_S\pi^+\pi^-$ and $K^0_S K^+K^-$. Phys. Rev.*, D78:034023, 2008.

[68] Tatiana Likhomanenko et al. *LHCb Topological Trigger Reoptimization. Journal of Physics: Conference Series*, 664(8):082025, dec 2015.

[69] Patrick Koppenburg. *Statistical biases in measurements with multiple candidates.* 2019.

[70] N. L. Johnson. *Systems of frequency curves generated by methods of translation. Biometrika*, 36(1-2):149–176, 06 1949.

[71] *Particle Data Group* . http://pdg.lbl.gov/2019/listings/rpp2019-list-D-zero.pdf.

[72] Muriel Pivk and Francois R. Le Diberder. *SPlot: A Statistical tool to unfold data distributions. Nucl. Instrum. Meth.*, A555:356, 2005.

[73] P. del Amo Sanchez et al. *Measurement of $D^0 - \overline{D}^0$ mixing parameters using $D^0 \to K^0_s\pi^+\pi^-$ and $D^0 \to K^0_s K^+K^-$ decays. Phys. Rev. Lett.*, 105:081803, 2010.